Development of singular solutions to the axisymmetric Euler equations

Alain Pumir[a] and Eric D. Siggia
Laboratory of Atomic and Solid State Physics, Cornell University, Ithaca, New York 14853-2501

(Received 24 July 1991; accepted 10 March 1992)

A variety of initially smooth axisymmetric flows with swirl are simulated with a variable mesh, finite-difference code with particular attention paid to the production of large (divergent) vorticity. Away from the symmetry axis, the evolution is entirely consistent with expectations based on the isomorphism with two-dimensional convection. Vortex sheets form on the leading face of "plumes" and their trailing edges roll up. When a "plume" begins to fission, a cusp develops at the cleavage point via a Rayleigh–Taylor-like instability and the maximum (three-dimensional) vorticity diverges, approximately, as inverse time squared. For technical reasons, the Boussinesq approximation was employed for this part of the simulation which observed, overall, a 10^6 increase in vorticity. The diverging strain was generated progressively more locally, justifying the approximation. Analytic estimates are provided which significantly constrain the singular solutions.

I. INTRODUCTION

Axisymmetric flows with swirl are one of the simplest physically realizable configurations, where genuine and potentially divergent vortex stretching can occur even though the velocity field is independent of ϕ in the cylindrical coordinate system (r,ϕ,z). This reduction in the effective dimension of the space renders more tractable the investigation of numerical problems requiring high resolution, in particular, as suggested by Grauer and Sideris,[1] the question of whether infinite vorticity can be created in a finite time when the viscosity is zero.

Our motivation for studying the initial value problem for the Euler equations is to learn how vorticity and strain couple to produce energy transfer to small scales.[2] One may also gain some insight into the underlying causes of the intermittency seen in three-dimensional turbulent shear flows.[3] Finite time blowup rather than exponential growth is merely a way of demanding that the stretching process be truly nonlinear. The imposition of axisymmetry replaces certain spacial gradients by $1/r$ (see below), and so renders the equations less singular when $r \geqslant r_0 > 0$. Since the full Euler equations have not yielded an acceptable singularity, and not for lack of resolution,[2,4] why investigate this special case?

There is the real possibility that singular solutions exist but are unstable, so that to observe them would require tuning the initial conditions. Axisymmetry is one form of tuning. It is enough of a simplification that one can derive stringent bounds which exclude certain processes, such as roll-up, as likely precursors to a finite time singularity. The opportunity to compute in two dimensions is also essential since to reach the asymptotic regime requires passing through a "transient" during which the vorticity grew by a factor of 100 but only exponentially. We were able, however, to go further and observe an additional $\sim 10^4$ growth in vorticity which is naturally fit by a finite time power law divergence.

Of more interest than the yes or no answer of whether a singularity exists is the mechanism for its formation. One's intuition for axisymmetric vortex dynamics is greatly enhanced by the analogy that exists with two-dimensional Boussinesq convection. Indeed, our candidate singularity occurs on or near the symmetry axis when the cap of a rising plume becomes unstable and begins to cleave in two. The convection analogy improves as the singularity grows, since the dynamics becomes more localized.

The following two sections (Secs. II and III) detail the equations, including their relation to Boussinesq convection, and the numerical methods used to solve them. They are somewhat involved since this problem cannot be touched without adaptive mesh techniques.

The numerical results in Sec. IV begin with simulations of the true axisymmetric equations pursued to moderate resolution for initial conditions whose extent in r is comparable to their distance from the symmetry axis. The analogy with convection is then of only qualitative relevance, but nevertheless, empirically furnishes a reliable guide to what happens. Nothing very novel occurs, but we show the data because we are unaware of any comparable work. The relevance here is to support our contention that general initial conditions evolve toward a regime where the Boussinesq equations apply quantitatively. The bulk of this section (Sec. IV C) details the Boussinesq results. The graphical output we present begins where the axisymmetric runs ended, namely with a well-developed (i.e., maximum temperature gradient $\geqslant$curvature of cap) thermal plume. Since we run over such a large range of scales, $\sim 10^6$, and the singularity is approached so rapidly [length $\lesssim (t^*-t)^2$], the outer scales are effectively frozen as the innermost collapse. But the collapse is never steady (shape invariant), so it leaves behind an elaborate chain of partial roll-ups and incipient Rayleigh–Taylor "fingers" that our graphics record.

Section V contains a number of analytic bounds that

[a]Permanent address: Ecole Normale Supérieure, Laboratoire de Physique Statistique, 24 rue Lhomond, 75231 Paris, France.

 0899-8213/92/071472-20$04.00

corroborate and enhance the plausibility of our numerical findings. We show that the curvature of the cap must diverge if there is to be a finite time singularity, and that roll-up is not dangerous in this regard contrary to the results for a vortex sheet. We also include a stability calculation which shows that the bubble cap first becomes unstable where expected.

Section VI concludes by recapitulating our methodology, the evidence in favor of a finite time singularity, and its properties. Comparison is made with several other blowup problems. The Appendix demonstrates the convergence of our algorithms with mesh refinement.

II. GOVERNING EQUATION

For a ϕ-independent velocity, the Euler equations read

$$\partial_t(rv_\phi)+v_\parallel\cdot\nabla(rv_\phi)=0, \tag{1a}$$

$$\partial_t\mathbf{v}_\parallel+v_\parallel\cdot\nabla\mathbf{v}_\parallel=(1/r^3)(rv_\phi)^2\hat{e}_r-\nabla p, \tag{1b}$$

$$(1/r)\partial_r(rv_r)+\partial_z v_z=0, \tag{1c}$$

where

$$\mathbf{v}_\parallel=(v_r,v_z), \quad \nabla=(\partial_r,\partial_z),$$

and $\hat{e}_r$ points radially outward in a right-handed coordinate system (r,ϕ,z). Equation (1b) can be rewritten in terms of $\omega_\phi=\partial_z v_r-\partial_r v_z$ as

$$\partial_t(\omega_\phi/r)+v_\parallel\cdot\nabla(\omega_\phi/r)=-(1/r^4)\partial_z(rv_\phi)^2, \tag{2}$$

and in analogy with two dimensions, $v_\parallel$ is calculated from ω_ϕ via a streamfunction

$$v_r=-(1/r)\partial_z\psi, \quad v_z=(1/r)\partial_r\psi, \tag{3}$$

and a Poisson equation,

$$r\partial_r[(1/r)\partial_r\psi]+\partial_z^2\psi=-r\omega_\phi. \tag{4}$$

The other components of vorticity are $\omega_z=(1/r)\partial_r(rv_\phi)$ and $\omega_r=-\partial_z v_\phi$. The advection may be replaced everywhere by a Jacobian

$$v_\parallel\cdot\nabla\theta\rightarrow\frac{1}{r}\frac{\partial(\psi,\theta)}{\partial(r,z)}, \tag{5}$$

which makes the invariance of the integral, $\int r\,dr\,dz$ manifest.

The conservation of circulation, computed for loops defined by $\phi\epsilon(0,2\pi)$ at fixed (r,z), is expressed by (1a). When $v_\phi=0$, the vortex lines are closed and labeled by ω_ϕ, so their material transport by the flow is expressed by the conservation of ω_ϕ/r in (2). The regularity of ω_ϕ then follows nearly as in two dimensions. Note by analyticity $v_\phi\sim r$, and $\omega_\phi\sim r^2$ as $r\rightarrow 0$. The source term for ω_ϕ/r in (2) may be understood by imagining initial conditions with $\omega_\phi=0$ and $v_\phi(r)\neq 0$, i.e., a bundle of vortex lines in (r,z). The differential rotation implied by $v_\phi(r)$ leads to the generation of ω_ϕ.

In the absence of symmetry, the production of vorticity is expressed as vorticity times strain and so possesses one more derivative than the right-hand side of (2). The production of the r and z components of vorticity from (1a) is, at least at the level of counting gradients, unchanged.

There is a very informative analogy between the axisymmetric flow equations (1a)–(1c) and two-dimensional Boussinesq convection with the centripetal force replacing buoyancy and "gravity" radially outward. The correspondence is exact when the axisymmetric flow is confined to narrow annulus; $r_1\leqslant r\leqslant r_2, (r_2-r_1)/r_1\ll 1$. To make this apparent we rewrite (1a) and (2) as

$$\partial_t V+\frac{1}{r}\frac{\partial(\psi,V)}{\partial(r,z)}=0, \tag{6a}$$

$$\partial_t\Omega+\frac{1}{r}\frac{\partial(\psi,\Omega)}{\partial(r,z)}=-\frac{1}{r^4}\partial_z V^2, \tag{6b}$$

where $V=rv_\phi$, $\Omega=\omega_{\phi/r}$ and ψ is still obtained from (4).

Now set $\frac{1}{2}r^2\rightarrow\frac{1}{2}r_0^2-y$, $z\rightarrow x/r_0$, $t\rightarrow t/r_0$, $V^2\rightarrow\theta$, and $\Omega\rightarrow-\omega$. Equations (4), (6a), and (6b) become

$$\partial_x^2\psi+(1-2y/r_0^2)\partial_y^2\psi=(1-2y/r_0^2)\omega,$$

$$\partial_t\theta+\frac{\partial(\psi,\theta)}{\partial(x,y)}=0,$$

$$\partial_t\omega+\frac{\partial(\psi,\omega)}{\partial(x,y)}=\frac{1}{(r_0^2-2y)^2}\partial_x\theta. \tag{7}$$

Clearly for $|y|\ll r_0^2$ we obtain Boussinesq convection, and in addition this limit is not singular: $2y/r_0^2$ is always compared with one. (The effective gravitational acceleration is $g\sim r_0^{-4}$.) As solutions collapse, the relevant range of (x,y) decreases so the approximation improves. Even when there is no collapse we expect to see $(rv_\phi)^2$ organize into plumes and mushrooms. (The possibility of solutions centered on $r=0$ merits attention, but is not considered here.)

III. NUMERICAL METHODS

We have implemented an adaptive mesh, finite-difference code, to treat axisymmetric flow which follows in many respects our simulations in three dimensions.[2] The mesh is separable and defined by analytic functions that map the intervals $0\leqslant r_0\leqslant r<\infty, -\infty<z<+\infty$ onto the unit interval $0\leqslant x,y\leqslant 1$. In practice it was convenient to use

$$r=r_0+c_1\{\cot(c_2)-\cot[\pi x+c_2(1-x)]\}, \tag{8a}$$

$$z=[c_3+c_4\cos(\pi y)+c_5\cos(2\pi y)]\cot(\pi y), \tag{8b}$$

where the c_i are adjusted to put the maximum resolution where desired. Extending the outer boundaries to infinity makes the boundary conditions trivial and can be done at minimal cost with the mappings (8a) and (8b). We typically used a 256^2 grid.

The equations were time stepped as in (6a) and (6b) since the conservation laws are explicit. Centered differences were employed throughout on a uniform mesh in (x,y) until sharp interfaces formed. Thereafter the TVD (total variation decreasing) scheme of Osher and Chakravarty was used in r and z separately for the advective terms to eliminate spurious oscillations.[5,6] Although these algorithms were designed for shock problems, we document

below (Fig. 10) that they perform equally well for our incompressible flow and eliminate the oscillatory instability of centered differences when used for a steplike profile. The Poisson equation (4), with $\psi=0$ on all boundaries, was inverted with the cyclic reduction method of Swartzrauber.[7] Time stepping was done with a Runge–Kutta–Fehlberg code that automatically adjusted step size.

At $r=r_0$ one-sided differences are used and the term involving $\partial\psi/\partial z$ is omitted from the Jacobian in order to ensure that $r=r_0$ acts as a streamline, i.e., we assume a free-slip boundary. When $r_0=0$, we sidestep any complications involved at the origin by imposing initially $\omega_z(r=0)=\Omega(r=0)=0$. At infinity all quantities vanish.

With centered differences, it is possible to write the Jacobian in (6a) and (6b) so that the volume integral (defined by a trapezoid formula), of both the field and its square are conserved. Only the first power of the field could be conserved within the TVD scheme. Neither energy nor helicity (which reduces to $2\int V\Omega r\,dr\,dz$) is explicitly conserved by our finite-difference schemes, so their actual errors are a useful measure of the adequacy of the mesh.

It is well known that centered difference algorithms decouple the odd and even sublattices and are therefore susceptible to a slow buildup in grid scale oscillations; (N.B. the Osher–Chakravarty algorithm reduces to centered differences except where the gradient is large). This noise is confined to regions remote from the singularity, but to prevent it from growing, we have filtered V and Ω on the mesh separately in (x,y) according to the formula $u(i)\to 0.5u(i)+0.25[u(i+1)+u(i-1)]$. This filtering has minimal effect on derivatives which we quantitatively document when discussing our data. This smoothing has the additional benefit of providing an explicit measure of the adequacy of our resolution. Clearly with an arbitrary fine mesh, nothing would change if we averaged every point with its neighbors.

The smoothing was applied, with one exception, only when it became necessary to adjust coordinates which we did by cubic splines. There was always more than adequate resolution in the large gradient regions to prevent any oscillations in the spline interpolations.

In order to maintain the region of interest where the mesh is optimal, we occasionally added a "wind" from infinity defined by the streamfunction

$$\psi^\infty=(r^2-r_0^2)(v_z^\infty/2-v_r^\infty z/r_0). \tag{9}$$

The velocity field defined by ψ^∞ is irrotational, but does produce a constant stretching when $v_r^\infty\neq 0$ because of the cylindrical geometry.

The Boussinesq equations for $-\infty<x,y<\infty$ and gravitational acceleration/temperature$=-\hat{e}_y$ were discretized and time stepped by the algorithms just described. The "wind" from infinity that we added to maintain the center fixed simplifies because of the translational symmetry and does not add any stretching. A second more significant technical simplification in the Boussinesq limit is the ease of making a uniform dilation of coordinates.

Denote the unscaled vorticity, streamfunction, and temperature by ω, ψ, and θ, respectively, and their scaled versions by capitals. Then

$$\Omega(\mathbf{x}/a,T)=\omega(\mathbf{x},t)/b,$$

$$\Psi(\mathbf{x}/a,T)=\psi(\mathbf{x},t)/(ba^2),$$

$$\Theta(\mathbf{x}/a,T)=\theta(\mathbf{x},t), \tag{10a}$$

where T is a rescaled time to be defined, and $a\to 0, b\to\infty$ as a function of time as a singularity is approached. To keep the gravitational acceleration constant we set $ab^2=1$. The equations then read

$$\partial_T\Theta+\alpha\mathbf{X}\cdot\nabla_X\Theta+\frac{\partial(\Psi,\Theta)}{\partial(X,Y)}=0,$$

$$\partial_T\Omega+\alpha\mathbf{X}\cdot\nabla_X\Omega+\frac{1}{2}\alpha\Omega+\frac{\partial(\Psi,\Omega)}{\partial(X,Y)}=\partial_X\Theta, \tag{10b}$$

with the definitions

$$\nabla_X^2\Psi=\Omega,\quad \alpha=-\partial_T\ln a,\quad \partial_T t=a^{1/2}. \tag{10c}$$

The one free parameter in (10a)–(10c) is $\alpha(T)>0$ which was piecewise constant and adjusted by hand to maintain the resolution of the coordinate mesh around the singularity fixed as the solution in unscaled variables collapsed. The length scale a and real time t are integrated along with (10b) and then used to recover the physical fields ω and θ via (10a). For example, if

$$\lim_{T\to 0}\frac{1}{T}\int_0^T\alpha=\bar{\alpha}>0$$

exists and Θ,Ω remain smooth order one functions of X and T, then $|\nabla_x\theta|$ blows up in a finite time t^* as $(t^*-t)^{-2}$. Similar methodology was used in Ref. 8. [Actually (10a)–(10c) is not the most general rescaling possible, but was the one we implemented, see Sec. VI.]

For future reference, we note how to recover from a Boussinesq simulation [i.e., (7) or (10)], the vorticity $(\omega_r,\omega_\phi,\omega_z)$, in the axisymmetric problem when (r,z) in the latter can reasonably be approximated by rectangular coordinates (y,x), respectively. From the correspondence used to obtain (7) we have an effective $g=r_0^{-4}$ and

$$(\omega_r,\omega_\phi/r_0,\omega_z)\leftrightarrow-(\partial_x\theta^{1/2},\omega,\partial_y\theta^{1/2}), \tag{11}$$

where r_0 is some mean radius. The Boussinesq approximation allows us to add an arbitrary constant to θ to keep it positive. Physically the variation of θ [or V^2 in (7b)] should be lumped with g to nondimensionalize the equations.

An impression as to the capabilities of our scheme for (6a) and (6b) is conveyed by Figs. 1(a) and 1(b) which compare the evolution of a vortex ring under our two differencing schemes. The initial ratio of radius to core size was sufficiently large so that locally the equations approximate 2-D Euler and the strain acting on the core is minimized so as to not generate any obvious instabilities. Nevertheless, the core shape does evolve since solutions

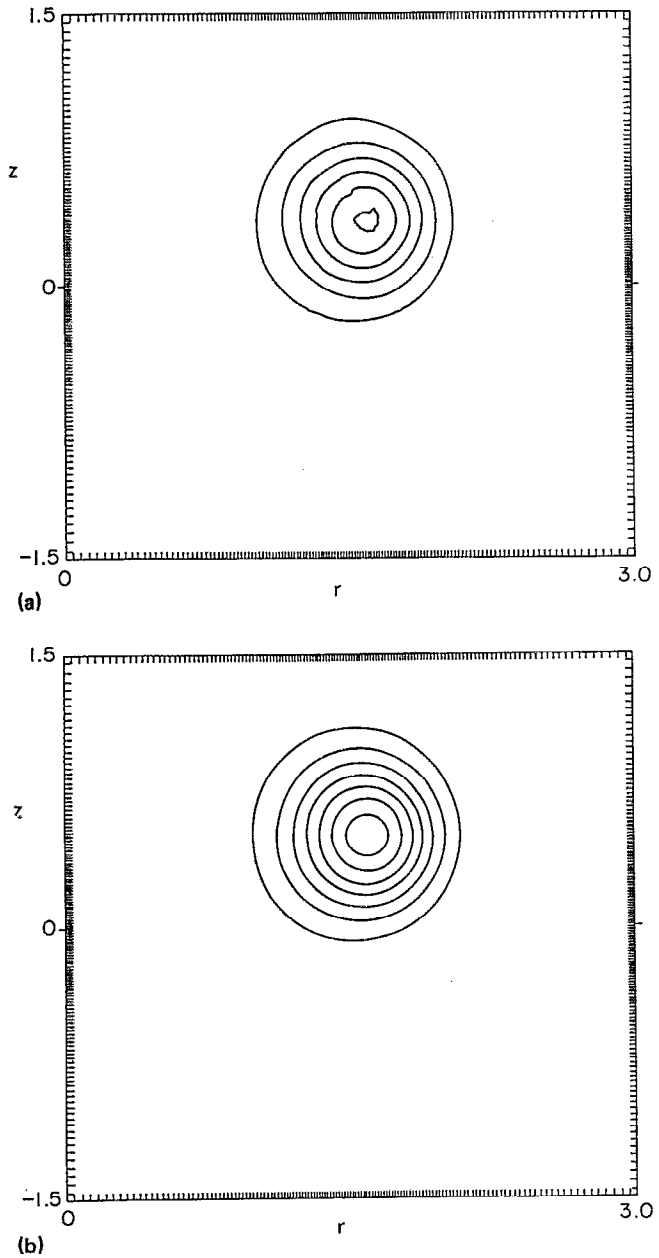

FIG. 1. Comparison of a vortex ring run with finite differences (a) and the TVD scheme of Ref. 6 (b). The mesh is shown by tics, and there is a negative velocity in z [cf. Eq. (9)] which maintains the ring approximately stationary in the vertical. The time of evolution times the ring velocity is approximately 3.5 core diameters. The energy, $\int\Omega^n, n=1,2,3$ and max ω_ϕ are (1.1313, 1.508, 0.754, 0.503, 3.012) initially and (1.1324, 1.510, 0.747, 0.495, 3.090) in (a) and (1.1315, 1.510, 0.724, 0.487, 2.995) in (b). In (a), the change in the first two moments of Ω is entirely due to remeshing the coordinates twice prior to the time shown.

stationary up to a translation are not easy to guess. The performance of the rescaling procedure is discussed in Sec. IV C.

We conclude this section with a remark on methodology. To achieve a 10^6 amplification in gradient required many remeshes. These tended to be quite minor when we used the continuous rescaling (10b) and (10c) but at the very least we had to verify graphically that the resolution remained adequate and adjust the exponent α. It is difficult to completely automate this procedure since the singular solution was by no means self-similar. An incidental benefit of this intervention was that it was easy to run with the old mesh past the remesh time. The two meshes were then compared, giving us confidence in our accuracy. Another mesh comparison is left for the Appendix.

IV. NUMERICAL RESULTS

This section has a twofold purpose. First, subsections A and B illustrate, for a variety of initial conditions, that axisymmetric flows evolve toward certain characteristic patterns: vortex sheets that roll up, or sharp fronts separating regions of different V^2. Both structures could have been anticipated from the Boussinesq analogy. The "fronts" are the central cap of a thermal plume or bubble on the edges of which vortex sheets form by virtue of the shear. Since our analytic estimates imply singularities are unlikely for roll-up, in the balance of this section (subsection C) we examine in detail the tip of a plume within the Boussinesq approximation and find a singularity.

A. Initial evolution and roll-up

We have restricted our attention to flows that can sensibly be defined for $r_0>0$ and in that class, the vortex ring is trivial because $V\equiv 0$. Although we have run a whole spectrum of initial conditions with increasing V, the essential mechanism for the generation of Ω is most clearly understood by starting with an "axisymmetric jet," $\Omega=0$, and V a Gaussian centered at a nonzero radius.

Shortly after $t=0$ in Figs. 2(a) and 2(b), we see the formation of the characteristic dipole pattern in Ω driven by $\partial_z V^2$ that clearly is antisymmetric around $z=0$. This vortex dipole translates radially outward. The signs appear reversed since the proper right-handed coordinate system is defined by (r,ϕ,z) not (r,z,ϕ). At later times, the region of maximum V pushes forward (Fig. 3) as one expects from the Boussinesq analogy, and a shell or cap is formed [Figs. 4(a) and 4(b)]. In Fig. 4(b), the loci of $\Omega=0$ for $z>0$ closely follows the curve of $\partial_r V$; Ω itself is predominately negative but can evidently reverse sign. The same advection which concentrates V into a sheet acts on Ω and Fig. 4(b) shows the roll-up of that sheet together with overall rotation in the patch of negative vorticity formed earlier.

The maximum total vorticity, which includes the r and z derivatives of V, is located along $z=0$. In the present run we have deliberately kept the resolution in r uniform over the region displayed to better treat the roll-up and sacrificed resolution in the cap that we will reexamine below. At its maximum along $z=0$, ω is along $\hat{z}$ and the largest component of the rate of strain tensor is in (r,ϕ) since it involves the r derivative of V which is becoming discontinuous. By symmetry for $z=0$, the directions of maximum stretching and compression are perpendicular to $\hat{z}$ while the relative stretching along $\hat{z}$ or ω tends to zero. We therefore find precisely the same tendency toward two-dimensionality as was seen in our 3-D Euler simulations[2] and elsewhere.

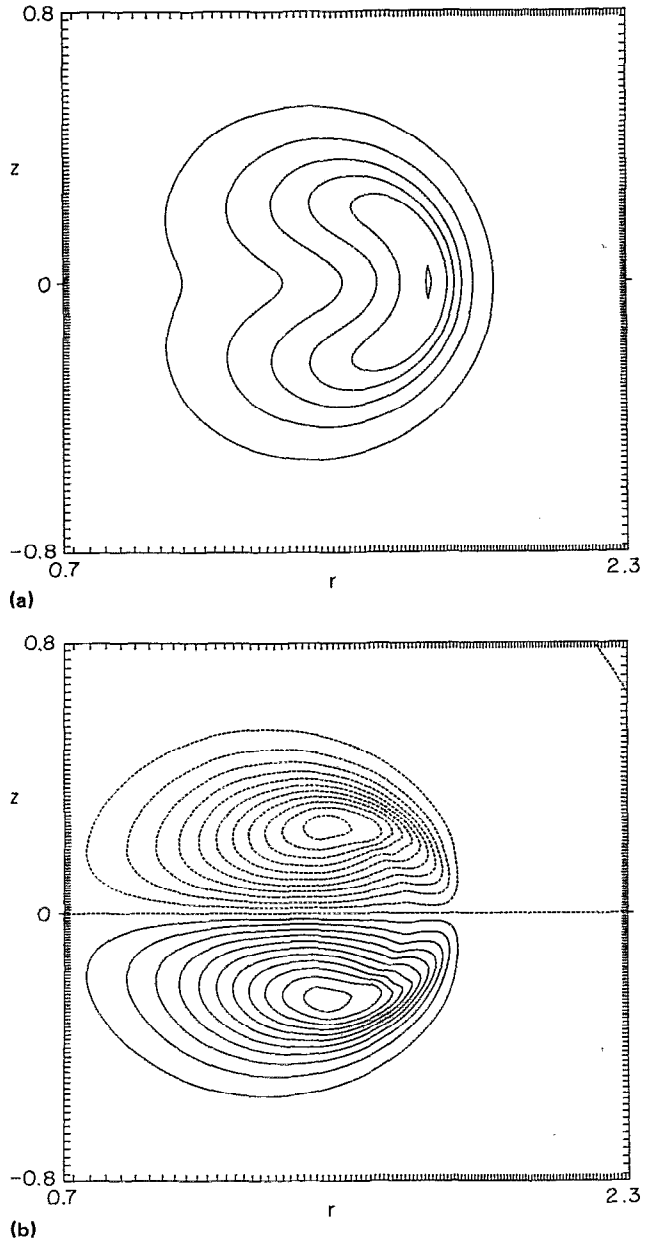

FIG. 2. Contour plots of V (a) and Ω (b) for the axisymmetric jet at $t=4$ that began as a Gaussian in V centered at $r=1.2$ and $z=0$ with a lowest contour level of radius=0.53, and $\Omega=0$ [cf. Eqs. (6a) and (6b) for the definition of V, Ω]. The contour interval is 0.1 in (a) and (b). Strictly positive values are solid, and the solid horizontal contour in (b) is zero.

When Ω is nonzero initially, the same phenomena are seen: formation of a bubble and roll-up of its edges with some superimposed net rotation and translation. We therefore idealized our initial conditions somewhat further to focus either on the cap of a bubble or the roll-up and suppose that any Ω added initially is not essential to the formation of a singularity which has to involve large gradients in small regions.

To produce roll-up without creating a bubble, we took V constant from the inner boundary $r=r_0$ out to some $\bar{r}_+$ for $z\gtrsim 0$ and $\bar{r}_-$ for $z\lesssim 0$ with $\bar{r}_+>\bar{r}_-$ and then decreased V to zero smoothly in the r and z directions and in

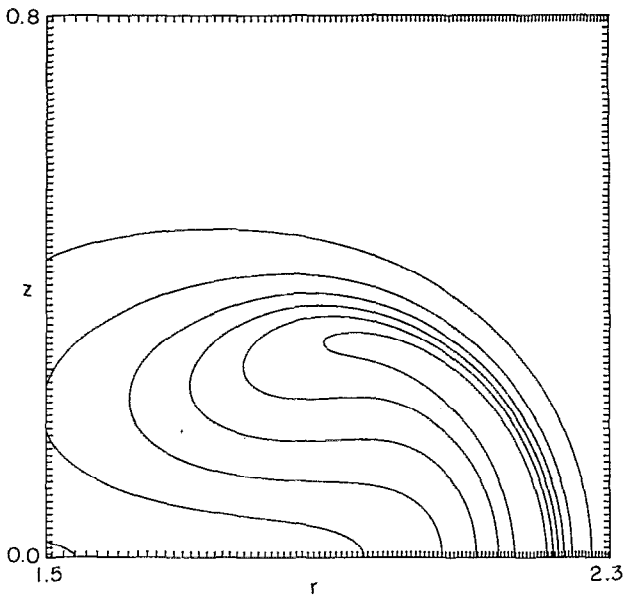

FIG. 3. Continuation of Fig. 2(a) at $t=6$. Only $0\leqslant z$ needs to be shown by symmetry. The spatial differencing is done by the TVD scheme of Ref. 6.

particular along the step $z=0$, $\bar{r}_-\leqslant r\leqslant\bar{r}_+$. For $|z|\to\infty$, both $\bar{r}_\pm\to r_0$ and $V\to 0$ so as to satisfy the boundary conditions. The initial vorticity was zero. Figures 5(a) and 5(b) show that the step generates vorticity which acts to accentuate the overhang. At later times [Figs. 6(a) and 6(b)], we see the roll-up develop without there yet being substantial enough regions of $\partial_z V<0$ to make $\Omega<0$ anywhere. Not much vortex amplification has occurred, $|\boldsymbol{\omega}|(t=24)/|\boldsymbol{\omega}|(t=0)=6$, and it is mostly due to ω_z or ω_r since $|\omega_\phi|(t=24)/|\boldsymbol{\omega}|(t=24)=0.28$. We have not followed this roll-up any further since the analytic arguments in Sec. V A convince us that no singularity is to be found.

B. Evolution of the bubble cap

To minimize the roll-up that developed for the "detached" bubble in Figs. 2–4 we initialized with Rayleigh–Taylor-like initial conditions consisting of a slowly tapering cylinder of $V>0$ which begins at the inner radius $r_0=10$ and extends out to $\bar{r}\sim 12.5$ where it decreases smoothly to zero. A slight bulge around $z=0$ replaces the step in Fig. 5(a) to encourage the formation of a circular cap. The initial evolution is shown in Figs. 7(a) and 7(b).

To control gradients that developed near r_0 we moved r_0 outward when we remeshed the coordinates. To verify that the growth of $\partial_r V$ is minimally affected, we show in Figs. 8(a) and 8(b) the most sensitive component of the strain before and after the first remesh where the errors are largest. The remeshing errors in Ω and the derivatives of V are conveniently controlled by monitoring $|\boldsymbol{\omega}|$ and appear in Fig. 9 as small steps.

The presence of an inner wall, removal of some circulation near r_0 with the coordinates changes, and the r^{-4} factor multiplying the buoyancy term in (6b) all contribute to making the velocity of the tip approximately con-

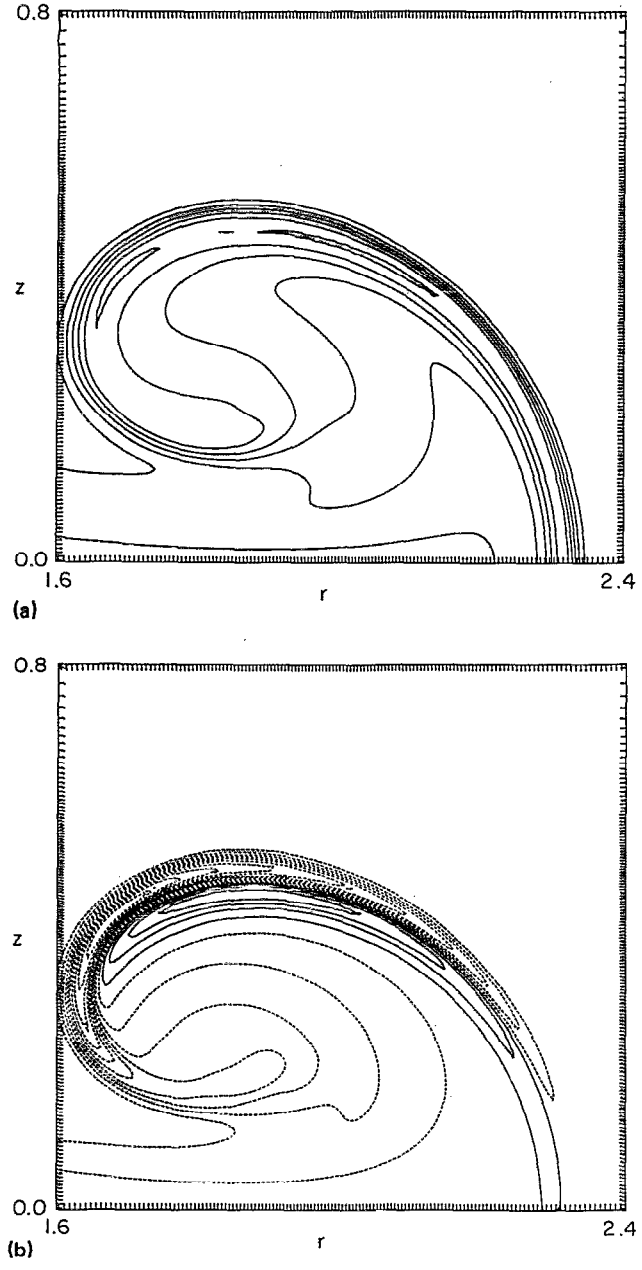

FIG. 4. Continuation of Fig. 3 showing contour plots of V (a) and Ω (b) at $t=10.5$. The maximum of $|\omega_\phi|$ is 5.6 vs 0 at $t=0$.

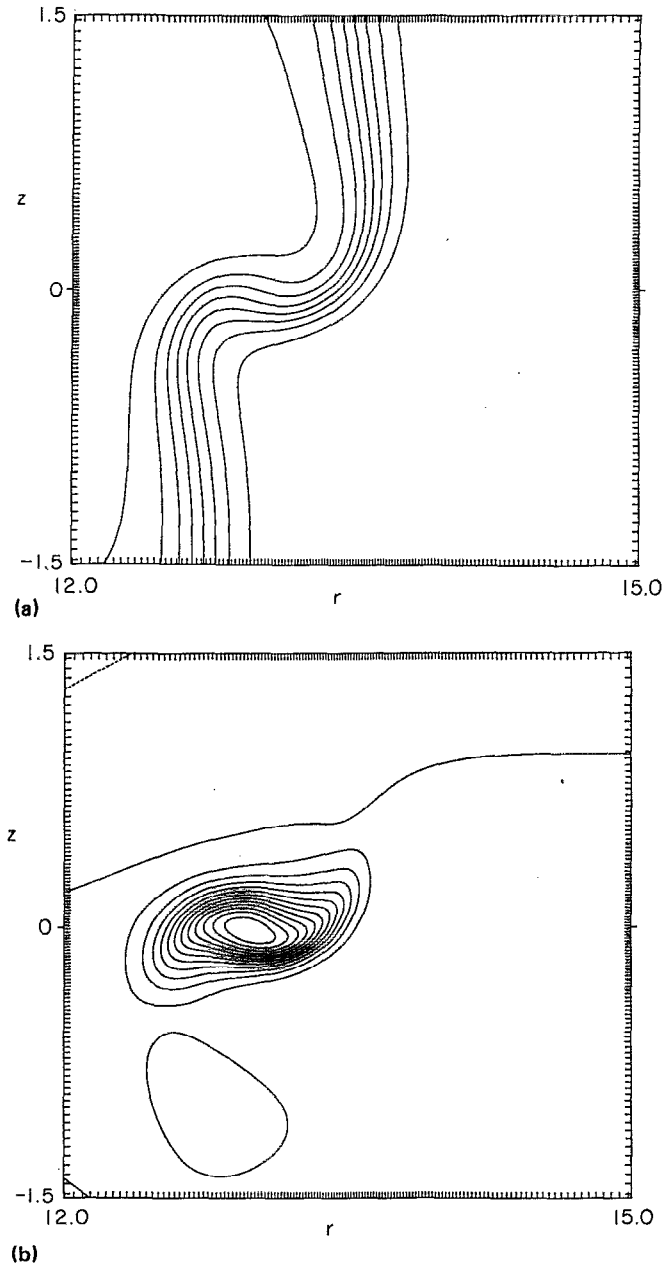

FIG. 5. Early evolution of step in V designed to stimulate a roll-up for V (a) and Ω (b) at $t=10$. The maxima of $(|\omega_\phi|, |\omega|)$ are (0,1.5) at $t=0$ and (0.84,2.3) here.

stant at long times in contrast to the constant acceleration observed for Rayleigh–Taylor between two semi-infinite spaces. We nevertheless believe the thickness and stability of the tip are correctly simulated because we have controlled the strain. The conservation properties of our numerical scheme are important here since both the advection and production of Ω are explicitly in conservative form so no spurious circulation can be produced even where the Ω responsible for the strain is far away and poorly resolved. Finally, just the cylindrical geometry will asymptotically make the tip velocity constant since the effective gravitational acceleration for Ω in (6b) is $\sim r^{-4}$ and $\int (\bar{r}+vt)^{-4}\, dt$ converges.

Figures 10(a) and 10(b) show the profile of V for the bubble at the time when exponential growth takes over (Fig. 9). As the interface between $V=cst$ and $V=0$ thins, a TVD scheme is essential to avoid oscillations as shown in Fig. 10. The surprising feature of Figs. 11(a) and 11(b) is the complete lack of any instability near the tip that could decrease the radius of curvature. If the curvature remained uniformly bounded in time, a finite time singularity is implausible, because as we show in the next subsection, the strain acting on the tip is bounded, implying exponential growth.

Nevertheless, a flat interface is Rayleigh–Taylor unstable as already remarked, and the relevant measure of "flatness" is interface thickness times curvature which is evidently quite small in Fig. 11(a). The instability calculation pertinent here is not completely trivial even for a flat in-

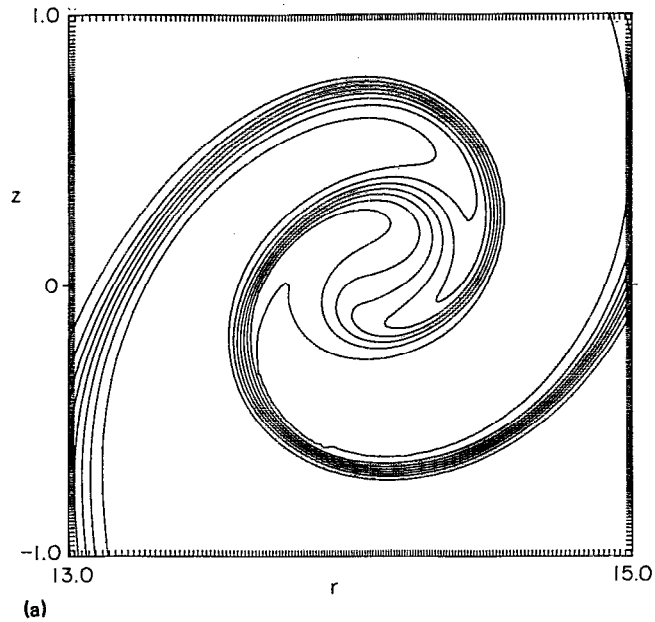

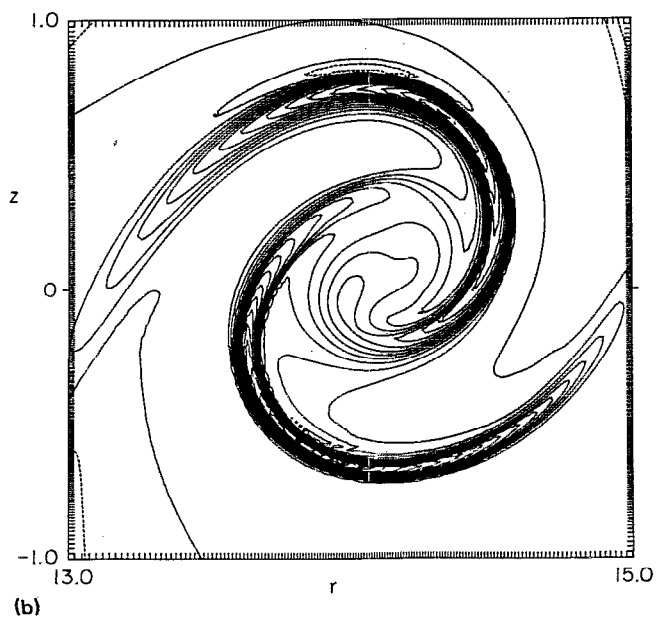

FIG. 6. Continuation of the data shown in Fig. 5 to $t=24$ showing V (a) and Ω (b). At this time, $\max|\omega_\phi|=3$ and $\max|\omega|=9.9$. A contour plot of $|\omega|$ would look more rolled up than (b) in the center.

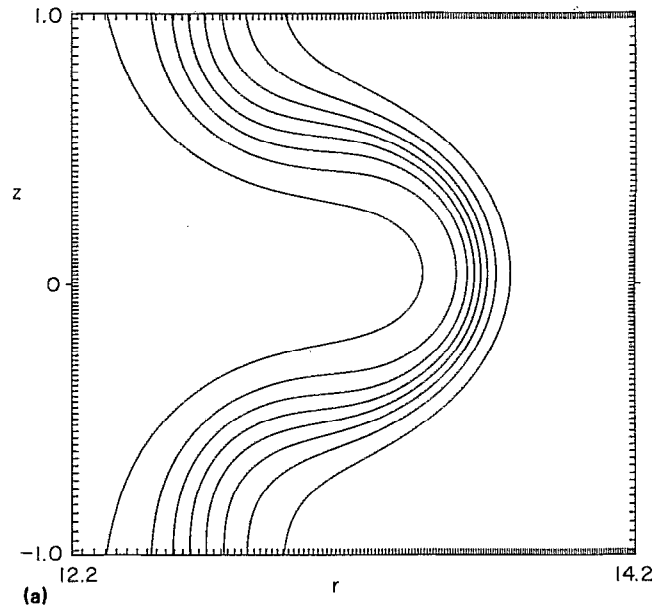

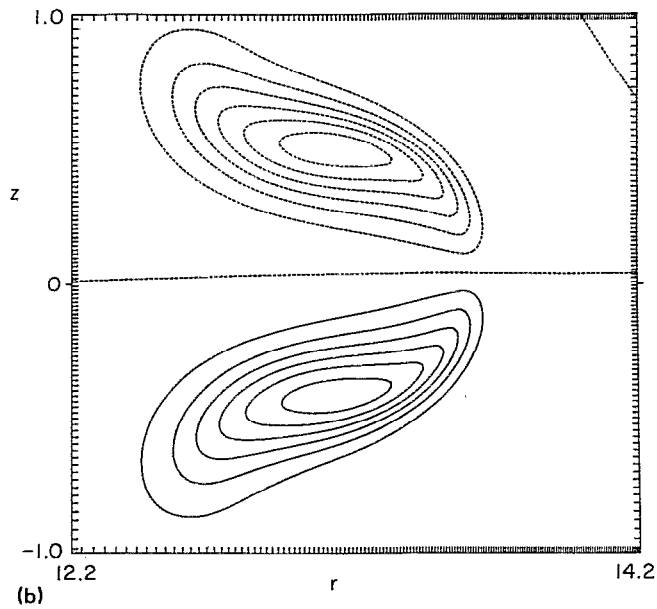

FIG. 7. Contour plots of V (a) and Ω (b) for $t=10$ and initial data chosen to favor a bubble (cf. Sec. IV B). The spacing between two contour lines is 1.0 (a) and 0.009 (b). A slight asymmetry between $\pm z$ was introduced to encourage any nonsymmetric instabilities.

terface because there is a superimposed strain which has a stabilizing tendency (cf. Sec. V B). In an effort to provoke an instability, we restarted the code at $t=17.0$ and zeroed the accumulated Ω, thereby leaving V similar to Fig. 11(a) but with no initial strain. Still, no instability was found out to $t=30.0$, where the effective Rayleigh–Taylor growth rate ($\sqrt{g/\delta}$, where δ is the interface thickness and g the gravitational acceleration), is $\gtrsim 1$.

C. Singular solutions for 2-D Boussinesq

To push the simulation of the bubble cap significantly further, we rewrote our axisymmetric code to handle the Boussinesq equations on the plane. This eliminates all boundaries, allows us to introduce a "wind" from infinity to center the solution without adding strain, and simplifies the task of continuously stretching coordinates. While a more flexible axisymmetric code could have been written, there was no assurance that interesting physics would emerge so we adopted the expedient of working in the Boussinesq limit. Since we will document that the dynamics of the collapse is local and robust we do not regard this as a significant approximation. More to the point, in Sec. V B we do the stability calculation semiquantitatively and show for our values that instability is not expected for the

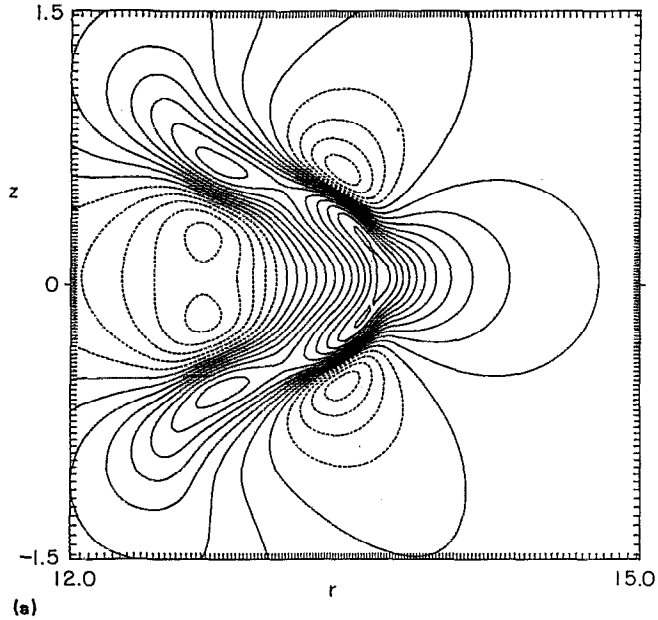

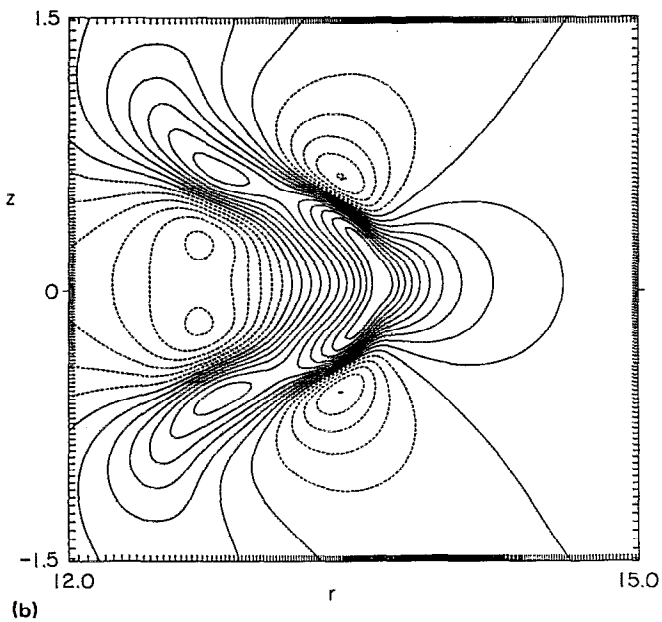

FIG. 8. Contour plots of $\partial_z v_z$ before (a) and after (b) the remesh for the same data as in Fig. 7. The contour interval is 0.02, and $\partial_z v_z$ varies from -0.1 to 0.22 in (a). The innermost contour near the tip has been lost after the remesh. The comparison of $\partial_r v_r$ is very similar.

times shown in Fig. 9, while it appears where expected in the Boussinesq simulations.

Our initial data was an isolated "hot" bubble with temperature distribution

$$\theta=(1+0.2y)/(1+x^2+y^2)^2. \tag{12}$$

The gravitational acceleration, $g=1$ [cf. Eq. (10b)] sets the time scale. The coordinates were adjusted by hand for the earlier runs since the solution was not self-similar enough to allow a uniform dilation. In the subsequent figures, $\omega\equiv\omega_z$ (Boussinesq) should be compared with ω_ϕ or Ω. The other vorticity components in the axisymmetric geometry, which in fact will diverge approximately as ω^2, are calculated from the gradients of θ via Eq. (11).

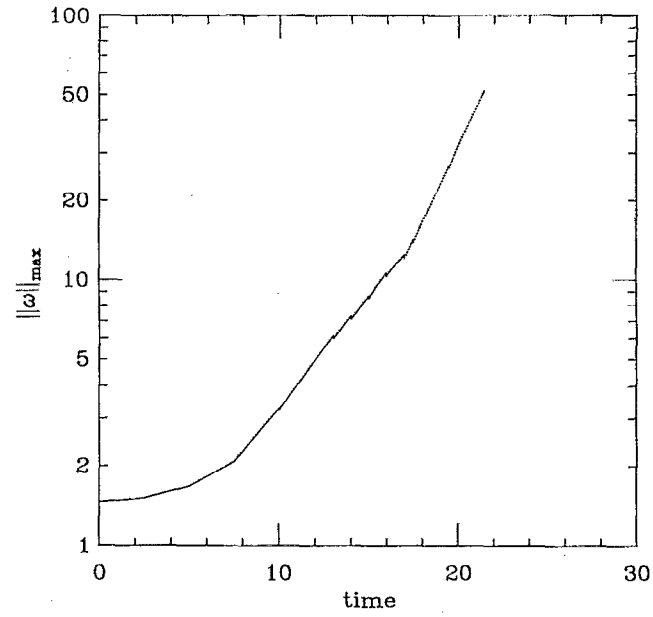

FIG. 9. Evolution of the maximum of the total three-dimensional vorticity for the bubble shown in Figs. 7(a) and 11(a). The small steps indicate the errors caused by the remeshing. The dotted line shows data obtained with an inward wind from $r=+\infty$ [cf. Eq. (8)] added to maintain the bubble stationary. Because of the cylindrical symmetry this produces a fixed strain which adds a constant to the slope.

The development of the singularity is most readily monitored by the maximum of $|\nabla\theta|$ (Fig. 12), whose location defines the center of collapse. It is generally located on the symmetry line $x=0$ (except for $7.9\lesssim t\lesssim 9.3$ and $t\gtrsim 10.06$), where the resolution is highest and where

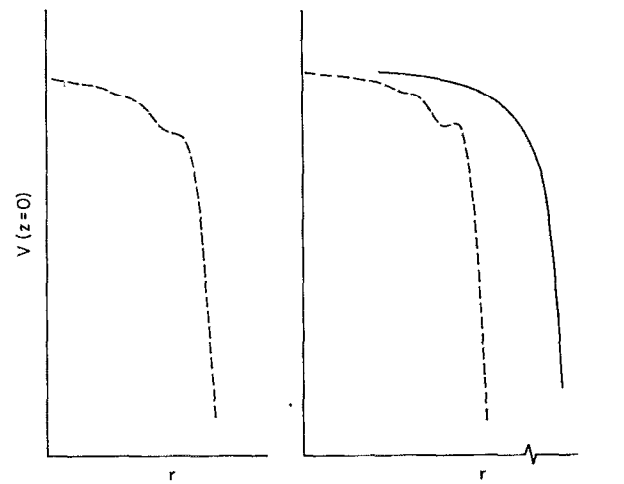

FIG. 10. Profile of V near the bubble tip [cf. Fig. 11(a)] for the data in Fig. 9 comparing centered differences (dashed line) and the TVD scheme (solid line). The data in the left panel at $t=15$, the last time for which centered differences were used, was restarted to give at $t=16$ the right panel. The two curves at the later time were offset for clarity.

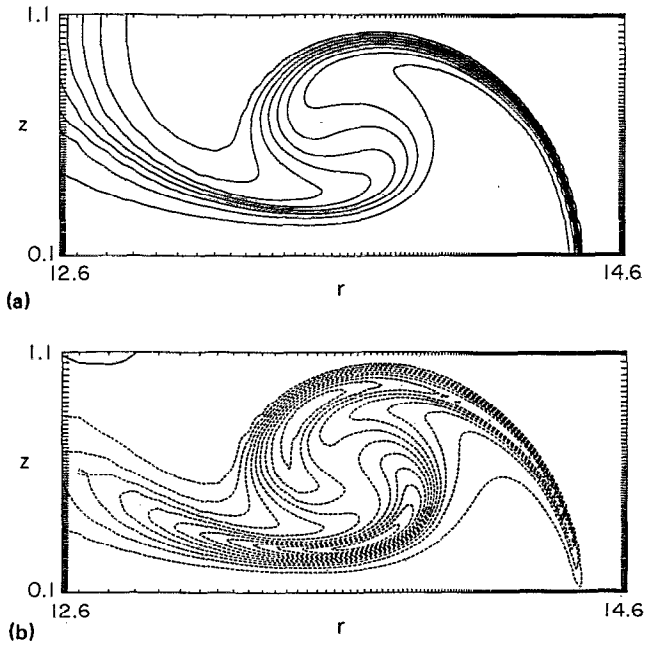

FIG. 11. Contour plot of V (a) and Ω (b) at $t=19$ for the run in Fig. 7. The symmetry line near the tip has drifted upward to $z=0.1$. The separation between contour levels is 1.0 (a) and 0.01 (b).

$|\nabla\theta| = -\partial_y\theta$. The maximum of ω, as will be apparent in the following figures, occurs well away from $x=0$ for $t \lesssim 9.5$ in a region that is less well resolved and affected by the large-scale cutoff (see below) and mesh changes. If the maximum vorticity near $x=0$ were plotted backward from $t\sim 10$, it would fall on a smooth curve below the one shown. Figure 12 is a convenient overview of what follows.

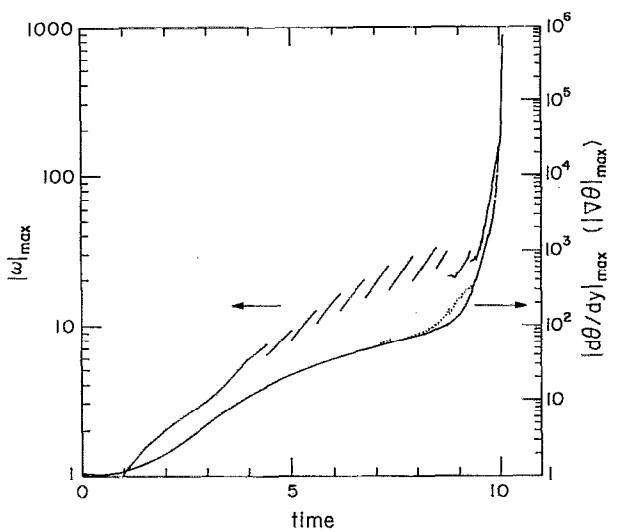

FIG. 12. The $\max_{x,y}(\omega)$, left scale; and max $|\nabla\theta|$, $\max_y \partial_y\theta$ $(x=0)$, right scale as a function of time. The discontinuities in the curves indicate coordinate changes as in Fig. 9. The max $|\nabla\theta|$ is shown as dotted and only deviates significantly from max $\partial_y\theta$ along $x=0$ around $t\lesssim 9.4$ where it drifts into a poorly resolved region and then jumps back. The ragged appearance of max ω for early times has a similar explanation (see the text).

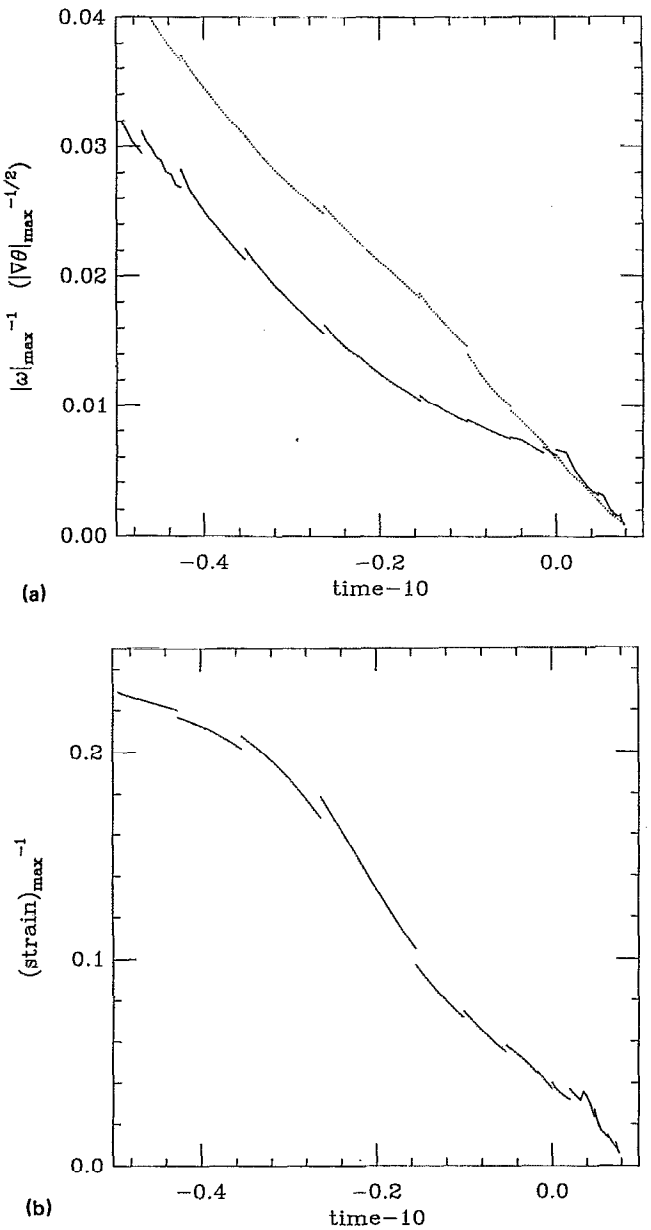

FIG. 13. Replot of the most singular portion of Fig. 12 (ω is solid, max $|\nabla\theta|$ dotted) (a); and the inverse of the rate of strain along $\nabla\theta$ at the point where max $|\nabla\theta|$ is maximum, $|\nabla\theta|^2/\Sigma_{ij}(\partial_i\theta\,\partial_i v_j\,\partial_j\theta)$ (b). The time is shifted by 10 for clarity. The "glitch" at $t\sim 0.04$ in (b) is real and associated with a jump in the location of the maximum.

For $0 < t \lesssim 8$ a shell forms as in Fig. 11(a) with curvature ~ 1, set by the initial conditions, across which θ jumps from nearly its maximum to 0. This follows closely what we saw previously and the growth in $|\nabla\theta|$ is exponential (compare Fig. 9).

An instability of the shell is just discernible around $t\sim 7.8$ and is associated with the rapid increase in $|\nabla\theta|$. Figure 13 shows that the growth plausibly terminates in a finite time singularity with crudely $|\nabla\theta| \sim 1/(t^*-t)^2$ and the strain along $\nabla\theta$ evaluated where $|\nabla\theta|$ is maximum;

$$\sum_{ij} \frac{\partial_i\theta\,\partial_i v_j\,\partial_j\theta}{|\nabla\theta|^2} \sim \frac{1}{(t^*-t)}.$$

The coordinate dilation algorithm [Eqs. (10a) and (10b)] was applied for $t \gtrsim 9.947$ by which time a well-defined approximately self-similar solution appeared around $x=0$.

The small jumps in the $|\nabla\theta|$ data show where the run was restarted, the coordinates adjusted, and some smoothing was done [cf. above Eq. (9)], to mix the odd–even sublattices. The smoothing was somewhat superfluous with the TVD algorithm that was used throughout but the decrease in max $|\nabla\theta|$ it causes, $\lesssim 5\%$, is an immediate check on the spatial resolution. The jumps in $\max_{x,y}(\omega)$ are typically smaller provided it falls in a well-resolved region.

The discontinuities in the maximum strain [Fig. 13(b)] are more pronounced and have a different origin. To accommodate the $\sim 10^6$ change in scale size we observe necessitates vastly expanding the mesh near the origin and pushing most of the temperature and circulation out toward infinity. For technical reasons we have to truncate the solution on the outer $\sim 5\%$ of the lattice points so that it tapers smoothly down to zero at infinity. This is done each remesh with the result that $\int\theta$ decreases from ~ 1 at $t=0$ to $\sim 10^{-6}$ at the end. Of more concern is the loss of vorticity and hence strain, which as we have defined it is just $\partial_t \ln(\max|\nabla\theta|)$.

Because the singularity is reached in a finite time, the vorticity produced at earlier times on the larger scales is effectively frozen with respect to the inner scales and has dipolar symmetry around $x=0$. Since the ratio of the innermost scale touched by the cutoff to $1/\max(|\nabla\theta|)$ was $\gtrsim 10^2$ when significant strain was lost, it is very reasonable to replace the truncated modes by a constant strain. We have confirmed this analysis by comparing contour plots of the strain, before and after applying the cutoff, which are identical up to an additive constant. Note that the loss of strain with cutoff is a quantitative measure of the locality of the dynamics. Near the final time, the cutoff hits modes with $|x|,|y| \gtrsim 2\times 10^{-4}$ in the units of Eq. (12); so, the Boussinesq approximation is indeed reasonable.

We chose not to compensate for the truncated vorticity so as to err toward damping the singularity. The complexity of the figures that follow make it evident that a simple straight line is not to be expected in Figs. 13(a) and 13(b). In particular the cusp around $t \sim 10.04$ is real. Nevertheless, Fig. 13(a) is persuasive evidence that the growth in $|\nabla\theta|$ is faster than exponential and most likely power law. It is instructive to compare the scale ranges in Figs. 12 and 13 with Figs. 5 and 6 of Ref. 2 which represent the most extensive data available in an unrestricted three-dimensional simulation.

The ostensible simplicity of Fig. 13 conceals an elaborate series of roll-ups that originate with the first instability of the shell (Fig. 14). On the largest scale, Fig. 14(a), the right half of the entire plume is shown. The differences with Fig. 11(a) are due to the initial conditions and axisymmetry; the plume in the earlier figure is attached to the inner radius of the computational domain. Also, the TVD algorithm is very diffusive where the resolution is poor, as in the outer regions of Fig. 14(a) (cf. the Appendix). On a finer scale in Figs. 14(b) and 14(c), the physics causing the instabilities becomes clear. The negative vortex concentrations around $x=0.25$, 0.45, and a third near $x=0.7$ (not shown), are indicative of a Kelvin–Helmholtz roll-up. The remaining vortex concentration around $x \sim 0.1$ has some dipole component suggestive of Rayleigh–Taylor physics; but, in reality, all instabilities when developed have a mixed character, there being both a vortex layer and heavy fluid over light. On physical grounds we believe the first instability is near $x=0$ and predominately Rayleigh–Taylor which then spreads to the vortex sheet.

By symmetry the vorticity vanishes for $x=0$ and the exterior flow is that of a stagnation point, converging along the y axis and diverging horizontally. This flow tends to suppress instabilities by decreasing their amplitude, increasing their wavelength (and hence decreasing their growth rate), and ultimately washing them into the rolled-up regions on the back of the plume. We show semiquantitatively in Sec. V B that these effects are responsible for making the quantity $|\nabla\theta|/\kappa$, where κ is the curvature of the cap, so large before instabilities are manifest. Finally on the finest scale, in Figs. 14(d) and 14(e), we see that there are no mesh-dependent instabilities.

[The term "instability" in this context must be understood in some Wentzel–Kramers–Brillouin (WKB) sense since the flow is not stationary prior to Fig. 14 (cf. Figs. 3–6). It is therefore unclear whether any external perturbation is needed to provoke the "instability" but if so, Sec. V B shows the requisite magnitude decreases as $\exp(-cst|\nabla\theta|^{1/2})$. The precise pattern in Figs. 14(a)–14(e) could depend on many small effects whose elucidation is immaterial to what follows since a quasistationary state never reforms. The literally minded reader may simply take Fig. 14 as our initial condition.]

A short time later (Fig. 15), the stronger of the two vortex concentrations in Fig. 14(e) has significantly rolled up, creating a characteristic pattern in θ [Fig. 15(a)]. A blowup of the inner region [Fig. 16(a)] suggests that the location of the maximum of $|\nabla\theta|$ is about to move back to $x=0$. Even though the x mesh in Fig. 16 was rather marginal and greatly refined on the next remesh, there is no suggestion of numerical problems even in the derivative. The jump in θ across the interface is 0.9 compared with the total variation of Eq. (12) along $x=0$ which is 1.005. Note that the curvature of the iso-θ lines has changed sign. The driving force for the blowup is almost purely Rayleigh–Taylor. The vortex sheet (note the magnification in y) in Fig. 16(b), whose sign is opposite to the predominant vorticity in Fig. 15(b), will now thin and spawn new roll-ups. Because of the disparity of scales, all the complex vortex structures in Figs. 14(c) and 15(b) reduce to a quasiuniform strain in Fig. 16(a).

Figure 17 shows that the roll-up in Eq. (15) has triggered another one above it and another below it, not shown in full. The numerical algorithms are evidently quite robust. The symmetry axis, $x=0$, is responsible for creating the large $\partial_x\theta$. A magnified view around $x=0, y=0.005$ would resemble Fig. 16 (see the Appendix).

In Figs. 18(a) and 18(b) we show on undistorted scales the shallow wedge or cusp that evolved from Fig. 16, but note the units. The mesh has been so refined that the

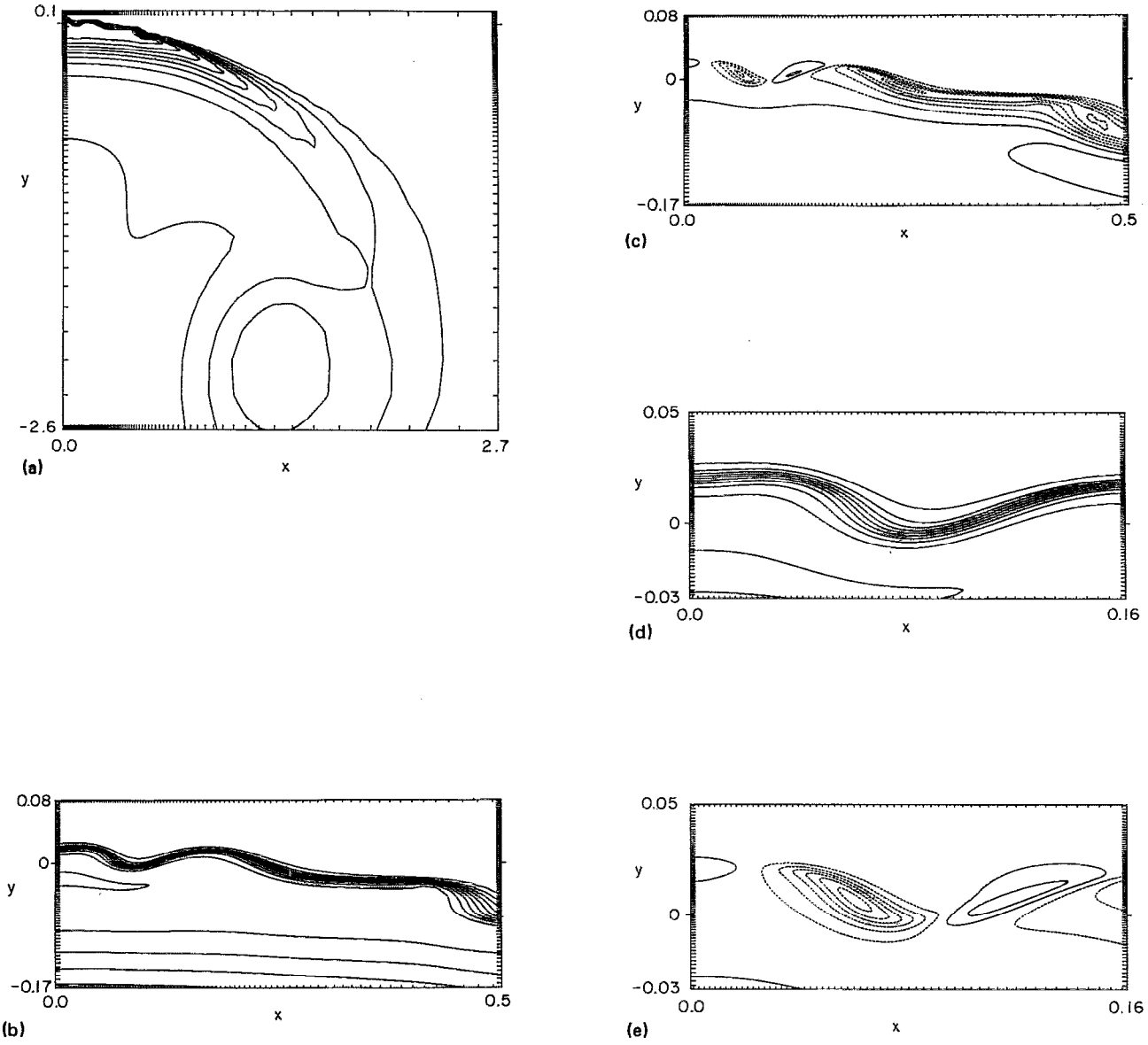

FIG. 14. The temperature θ [(a), (b), and (d)], and vorticity ω [(c) and (e)], at $t=8.754$ showing the development of the instability that disrupts the bubble cap; (N.B. θ is even and ω is odd under $x\leftrightarrow -x$). The contour interval for θ is 0.1 and θ increases gradually from 0 at $y=-\infty$ to hit 1.0 on its innermost contour and then jumps down by ~ 0.9 to zero at its leading edge. The contour interval of ω in (c) is 3.3, (range -19.9 to 3.3) and in (e) 2.2. The lowest solid contour is 0.

outermost x points shown are close enough to "infinity" that they are affected by the cutoff which explains the vertical contour lines of θ. The interface for large x is also thicker than it would be at higher resolution due to the TVD algorithm (cf. the Appendix). A magnified and vertically stretched view of the inner region shows two vorticity concentrations [Fig. 18(d)] and corresponding undulations in θ [Fig. 18(c)].

In Figs. 19(a) and 19(b) we show just the inner 25% of Figs. 18(c) and 18(d) at a time when the maximum $|\nabla\theta|$ moves to two symmetric points off the y axis. The curvature of the iso-θ lines near $x=0$ has again reversed sign [Fig. 19(c)], and the plume of cold fluid descending into the wedge has undergone a tip splitting, visible also in Fig. 19(d) as a bit of negative vorticity.

Near the final time (Fig. 20), we have recentered our coordinates to concentrate on one of two equivalent regions of max $|\nabla\theta|$. The computation is no longer symmetric under $x\rightarrow -x$. The slight dip visible in Fig. 19(c) evolves into the right-hand side of the maxima in Fig. 20(a). The jump in θ across the interface decreases from about 0.75 at $t=9.3$ to about 0.28 at the final time during which time max $|\nabla\theta|$ increases by ~ 6000.

Our numerical grid, as shown in the figures, telescopes rapidly inward to follow the singularity. Because the singularity is approached so rapidly, the large scales of flow in

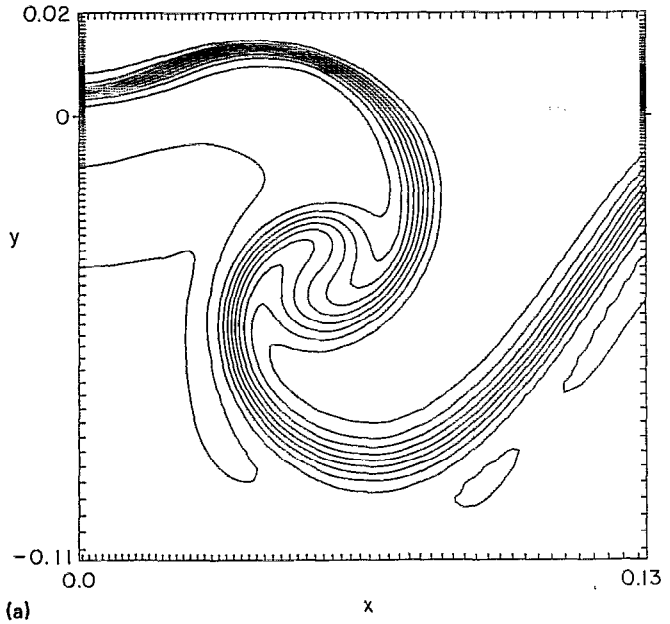

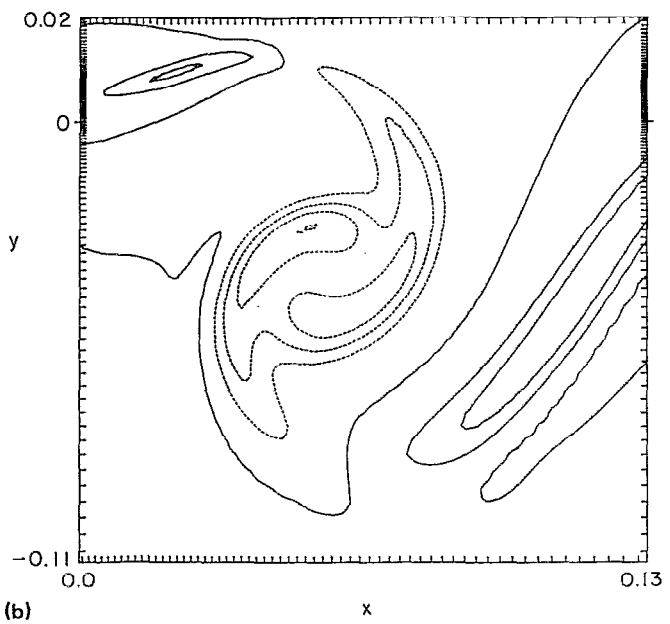

FIG. 15. A continuation of the run in Fig. 14 showing θ (a), and ω in (b) at $t=9.3$, $(\max|\nabla\theta|=243)$; θ varies from 0 for $y\gtrsim 0.015$ to 1.0 around $y\sim -0.03$ in units of 0.1; and ω varies from -26.4 to 13.2 in units of 6.6.

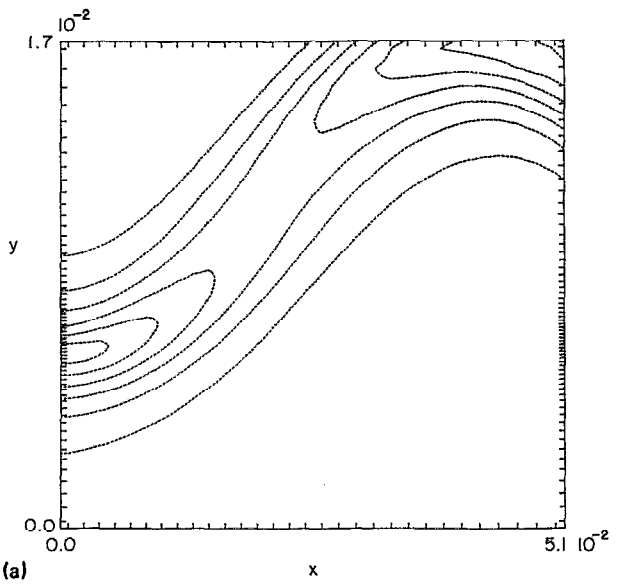

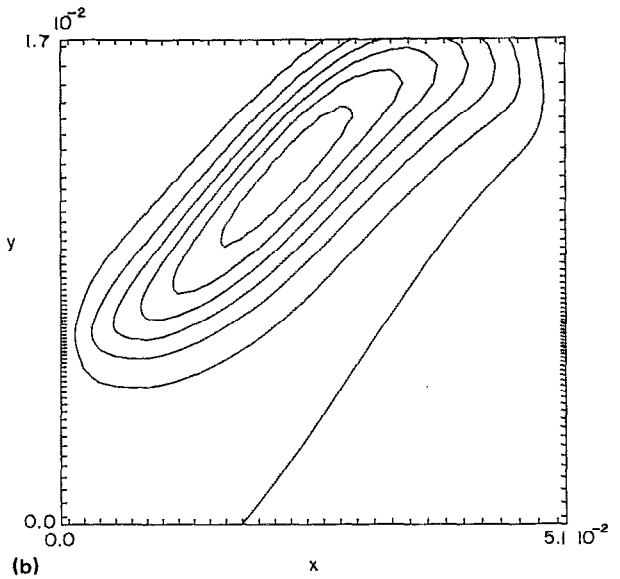

FIG. 16. A blowup of $\partial_y\theta$ (a) and ω (b) for the data plotted in Fig. 15 with the vertical scale magnified by 3 to make the y mesh visible. The gradient $\partial_y\theta$ varies from -218 to 0 in units of 36.3, and the vorticity varies from 0. to 13.2 in units of 2.2.

the earlier figures, insofar as they are pertinent to the singularity, are effectively frozen during the time which remains until the singularity is attained. Looking over our sequence of figures, it is apparent that they cannot be transformed into each other by adjusting scales. We return to this point in Sec. VI.

V. ANALYTIC ESTIMATES

A. Necessary conditions for a singularity

We now examine analytically how gradients in V (or θ in the Boussinesq case) generate the ϕ vorticity $\Omega=\omega_\phi/r$ (resp. ω). This will clarify a number of qualitative features in our numerics and provide a base from which to calculate the strain rate in (r,z). The time integral of the strain must diverge in a finite time if ∂V is to do likewise. To establish sufficient conditions for a singularity appears to require proving that a nontrivial equation actually has a solution, which seems hopeless. On the other hand, our bounds, which are nonrigorous, do make roll-up an improbable place to find a singularity for smooth initial data and suggest that a cusp is more likely—rather like what we find. We will work in the Boussinesq limit of (6a) and (6b) set $\mathbf{x}=(r,z)$ to facilitate writing equations, but retain Ω and V as dependent variables. Various multiplicative factors of r which become constants, $\bar{r}$, in the Boussinesq limit and were eliminated from (7) by a slightly different rescaling

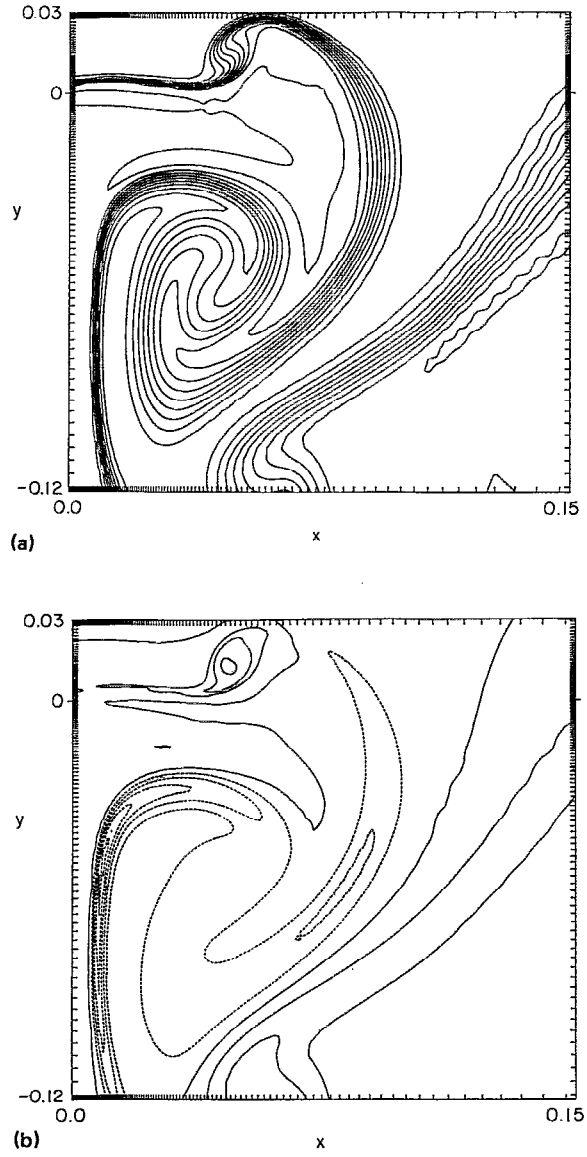

FIG. 17. Continuation of Fig. 15 at $t=9.736$ ($\max|\nabla\theta|=1.55\times10^3$). The range of θ is unchanged, i.e., $\theta(0,y\lesssim-0.01)\sim0.9$, and ω varies from -50.0 to 30.0 in units of 10.0. The cutoff has reduced θ to $\lesssim0.1$ for $|x|\gtrsim0.25$ or $y\lesssim-0.4$.

are retained here in order to keep dimensions and the connection with axisymmetry more explicit.

To firmly exclude the notion that (6a) and (6b) are somehow like 2-D Euler and therefore regular for all time, we note the following scaling ansatz for (6a) and (6b):

$$V=f\left(\frac{\mathbf{x}}{\tau^2}\right),\quad \Omega=\frac{1}{\tau}g\left(\frac{\mathbf{x}}{\tau^2}\right),\tag{13}$$

where $\tau=t^*-t$. It is "natural" in that it could be derived by supposing that the analog to (10a) and (10b) has a stationary solution with $\alpha=\text{const}>0$, as already noted. If the scale of the singular part of V is not preserved in time (e.g., the "jump" in V across the cap decreases), then one could have a solution $V=\text{const}+\tau^\eta f(\mathbf{x}/\tau^{2+\eta})$, $\Omega=(1/\tau)g(\mathbf{x}/\tau^{2+\eta})$. The (r,z) components of $\boldsymbol{\omega}$ always diverge more strongly than ω_ϕ. At the same level of naiveté, analysis of 3-D Euler implies $\boldsymbol{\omega}\sim\tau^{-1}g(\mathbf{x}/\tau)$, which is a stronger singularity than (13) since gradients do not have to be as large for blowup. Alternatively, the singular velocity scale is 1 for 3-D Euler but $O(\tau)$ based on v_r,v_z obtained from (13). The ansatz (13) is merely illustrative and will play no role in the remainder of Sec V.

Essential to our estimates is proper exploitation of Lagrangian coordinates in the (r,z) plane for one of which V itself is the natural choice. This will prove advantageous since $\partial_z V^2$ is the only source of Ω which otherwise is advected, i.e., remains constant in Lagrangian variables.

We illustrate these ideas by a trivial demonstration of the following useful lemma.

Lemma 1: The total circulation defined as $\int\Omega r\,dr\,dz=\int\omega_\phi\,dr\,dz$ within any closed contour line $V=cst$ is constant.

The proof is simply to integrate (6b) and observe no matter how convoluted the contour, the z integral of the right-hand side vanishes. This lemma is not a trivial corollary of Kelvin's theorem which pertains to the flux of $\boldsymbol{\omega}$ through a Lagrangian contour in 3D, since here the swirl does not uniformly rotate a curve $V=cst$ that initially is in a plane $\phi=cst$.

It immediately becomes apparent why in Fig. 4(b) $\Omega=0$ along the uppermost locus of $\partial_z V=0$ in Fig. 4(a). This locus consists of contour lines that initially were small circles around the maximum of V at $t=0$. [The breaks in the maximum contour line in Fig. 4(a) are indicative of numerical errors.] There is no net circulation within and minimal production of plus and minus Ω since $\partial_z V$ is uniformly small near a maxima.

A further refinement of Lemma 1 consists in calculating the circulation C within a contour defined by $V=V_0$ and a second Lagrangian variable λ which intersects V transversely and projects 1:1 onto $z=0, r_1\leqslant r\leqslant r_2$ as shown in Fig. 21. One finds

Lemma 2:

$$|\partial_t C|<\tfrac{1}{2}(V^2_{\max}-V_0^2)(r_1^{-2}-r_2^{-2})$$
$$\lesssim 2(V^2_{\max}-V_0^2)^2/(r_1^3|\nabla V^2|),\tag{14}$$

where $\nabla=(\partial_r,\partial_z)$. The second equality is not rigorous since it assumes V^2 is a quadratic function, but serves to emphasize the important tendency for $|\partial_t C|$ to decrease when approaching a singularity, $\nabla V^2\to\infty$. At the expense of further notation, one can readily write a formula for the circulation per unit λ in conservation form, $\partial_t(\partial_\lambda C)+\partial_\lambda j=0$, where j is the appropriately weighted integral over the "triangle" in Fig. 21. Lemma 2 can be applied to Fig. 4(b) with λ defined as the symmetry line $z=0$ to prove the total circulation for $z>0$ approaches a constant at the same rate the thickness of the cap goes to zero.

The two lemmas are rather global in that they refer to circulation within a region. A precise and useful formula for the velocity is readily established in what we will call the "contour dynamics limit" where we assume $\Omega=0$ initially and replace the continuous V^2 by a series of steps

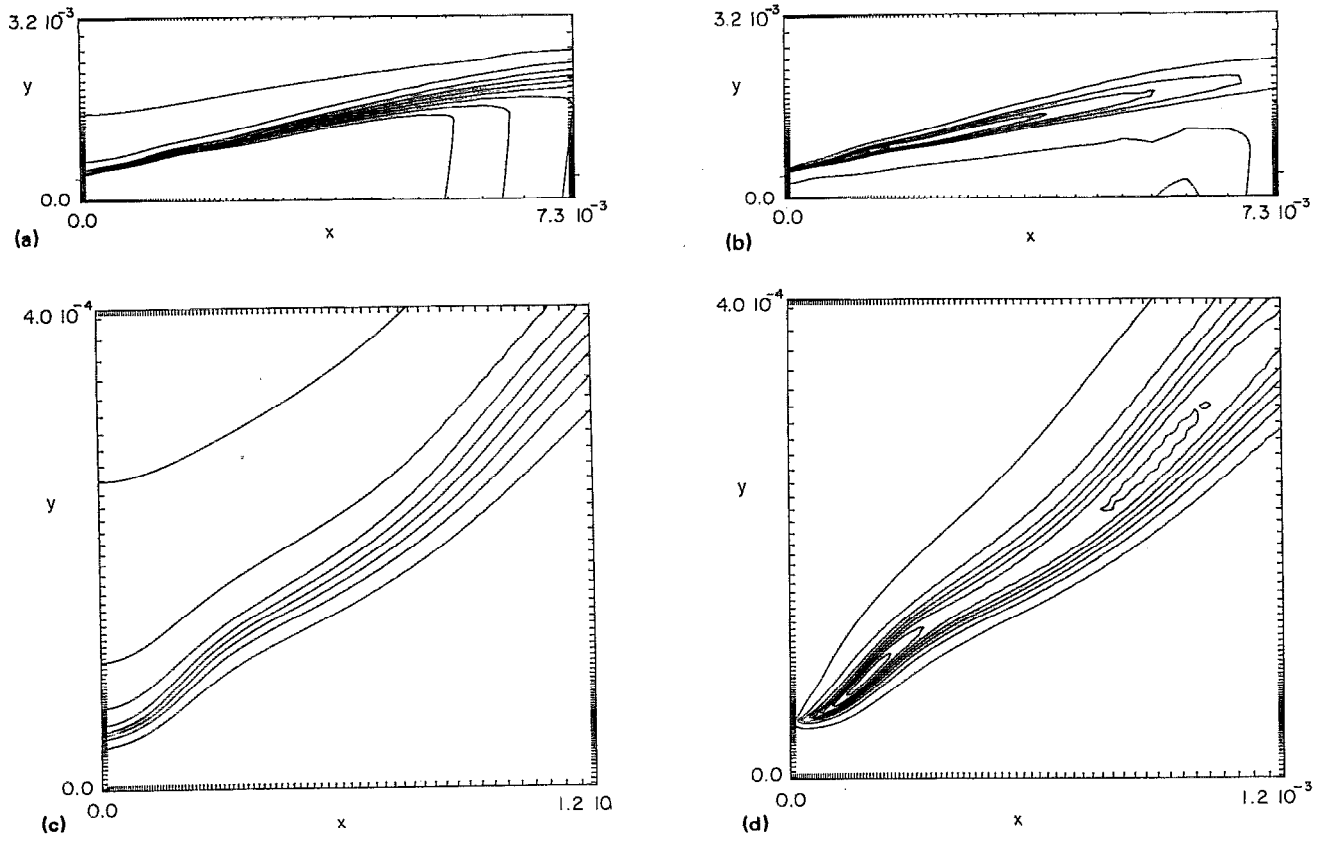

FIG. 18. Continuation of Fig. 17 showing the temperature θ [(a) and (c)] and ω [(b) and (d)] at $t=10.020$ (max $|\nabla\theta|=5\times10^4$). The vertical scale is magnified by 3 in (c) and (d). The contour interval is 0.1 for θ (range 0.1, 0.2–0.9), and 20.0 for ω (range 20–180).

each defined by some jump ΔV^2 along a contour $\mathbf{x}(\lambda,t)$, where λ is a Lagrangian marker. The Boussinesq approximation to Eqs. (4), (6a), and (6b) as defined in the beginning of this subsection reduces a complicated Green's function to a log. The velocity from one such contour reads $(i=r,z;g=\Delta V^2/\bar{r}^3)$,

$$v_i(\mathbf{x})=g\epsilon_{ij}\partial_j\int \ln|[\mathbf{x}-\mathbf{x}(\lambda,t)]|\gamma(\lambda)\frac{d\lambda}{2\pi},$$

$$\gamma=\int_0^t \partial_\lambda x_1(\lambda,t')dt', \tag{15}$$

where ϵ_{ij} defines the two-dimensional cross product. This is just the usual formula for velocity in terms of circulation density with γ computed from (6b) assuming V^2 is a step. Equation (15) could be used to construct a numerical scheme to time step $\mathbf{x}(\lambda,t)$.

A plausible estimate for the rate of growth of $|\nabla V|^2$ can be constructed from (15). It consists in calculating, locally, the strain rate from a bundle of nearly parallel steps in V^2 at a point within the bundle. We assume there is a single characteristic length along the level sets of V, which we take to be the inverse curvature, κ, and integrate only to this distance. By differentiating (6a) one finds

$$d_t|\nabla V|^2=-2\nabla V\cdot e\cdot\nabla V, \tag{16}$$

where d_t is Lagrangian and only the component of the strain, $e_{ij}=\frac{1}{2}(\partial_i v_j+\partial_j v_i)$, along the local normal $\hat{n}=\nabla V/|\nabla V|$ needs to be calculated from (15). To expand the integrand we require,

$$\partial_\lambda\mathbf{x}=s_\lambda\hat{t},$$
$$\partial_\lambda^2\mathbf{x}=s_{\lambda\lambda}\hat{t}+s_\lambda^2\kappa\hat{n}, \tag{17}$$

where λ is a Lagrangian variable along a step, $\hat{t}$ is tangent, and s is arclength. We find

$$\hat{n}\cdot e\cdot\hat{n}(x)=g\int\frac{\hat{n}\wedge(\mathbf{x}-\mathbf{x}')\hat{n}\cdot(\mathbf{x}-\mathbf{x}')}{(x-x')^4}\gamma(\lambda')\frac{d\lambda'}{2\pi}, \tag{18}$$

where $\mathbf{x}'=\mathbf{x}(\lambda',t)$ is the contour being integrated over (cf. Fig. 22). Expanding (18) around $\lambda=\lambda'=0$, and using $\lambda' s_\lambda\equiv y$,

$$\frac{\hat{n}\cdot e\cdot\hat{n}}{g}=\frac{1}{s_\lambda^2}\int\frac{[(\delta+\frac{1}{2}\kappa y^2)(\partial_\lambda\gamma)y^2+\frac{1}{2}\delta\gamma s_{\lambda\lambda}y^2/s_\lambda]dy}{D^2},$$

$$D=\left(\delta+\frac{1}{2}\kappa y^2\right)^2+\left(y+\frac{\frac{1}{2}s_{\lambda\lambda}y^2}{s_\lambda^2}\right)^2, \tag{19}$$

where $\delta=\boldsymbol{\delta}\cdot\hat{\mathbf{n}}$ can be of either sign and $s_\lambda=\partial_\lambda s$, etc. To eliminate superfluous complexity we will only need to work around the tip of the parabola where $s_{\lambda\lambda}=0$. However, our estimates would be dimensionally the same if we took $s_{\lambda\lambda}\sim\kappa s_\lambda^2$. The y integral in (19) is convergent, though for consistency we should assume $\kappa|y|\lesssim O(1)$. We finally in-

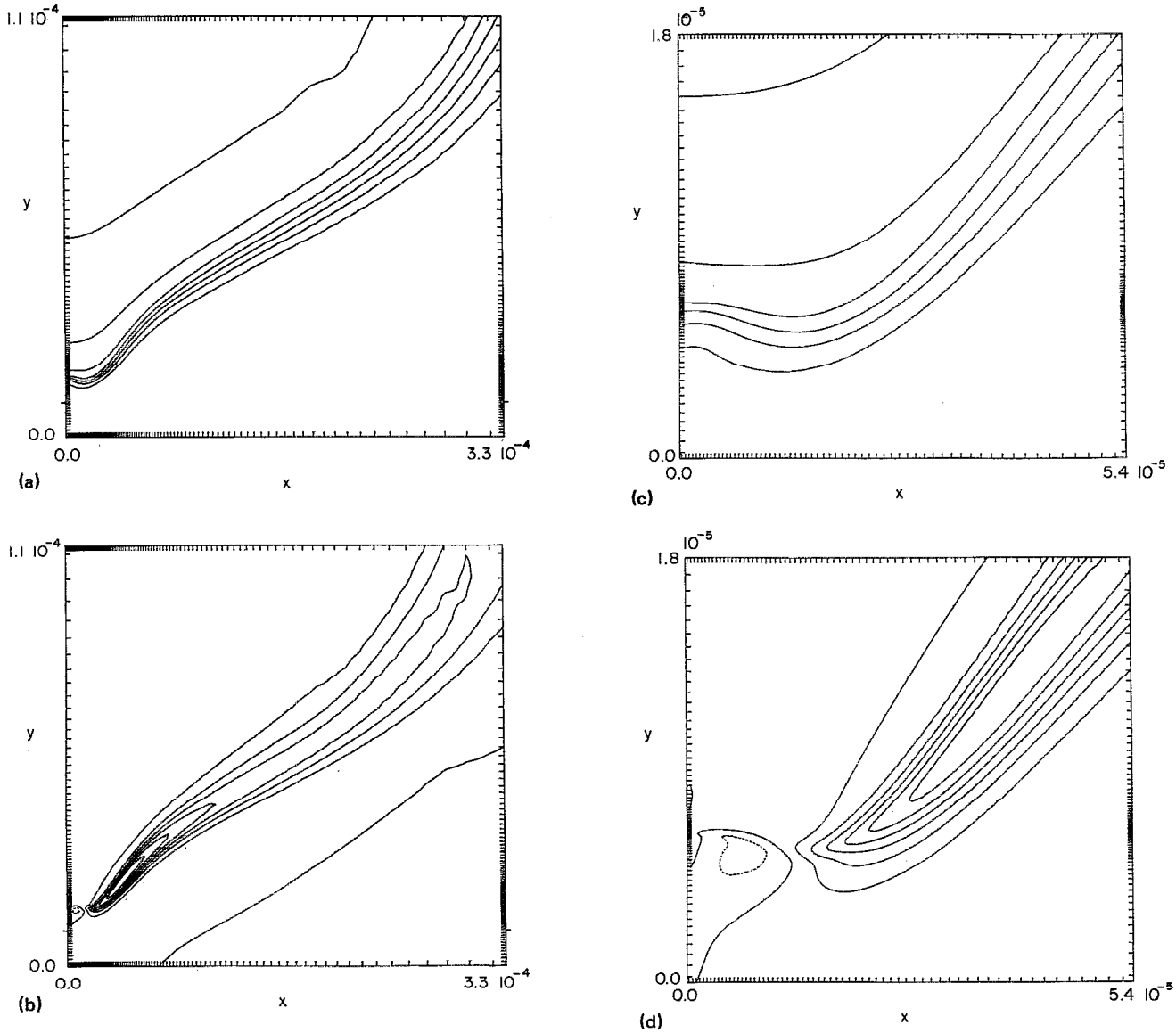

FIG. 19. Continuation of Fig. 18 showing the temperature θ [(a) and (c)] and ω [(b) and (d)] at $t=10.0646$ (max $|\nabla\theta|=3.7\times10^5$), with y magnified relative to x. The contour lines of θ run from 0.9 to 0.3 in units of 0.1 and those of ω from -74 to 444 in units of 74.

tegrate over $|\delta| \lesssim O(\kappa^{-1})$, which we parametrize in terms of the total jump in V^2 and exploit the conservation of the volume in a $\Delta\lambda,\Delta V$ rectangle in the form $s_\lambda/|\nabla V| = cst$ to rewrite (16)–(19) as

$$\partial_t(\nabla V)^2 \lesssim c \int_0^t \kappa(t')(\nabla V)^2(t')dt', \tag{20}$$

with c a generic constant. The time integral originates from $\partial_\lambda\gamma$ in (15) expanded as in (17) and the multiplicative $|\nabla V|^2(t)$ in (16) has canceled against the s_λ^{-2} prefactor in (19).

Equation (20) is the basis of our earlier assertion that blowup is impossible unless the contour lines of V fold as they squeeze together. To bound how rapidly $|\nabla V|$ diverges if there is blowup, we assume on physical grounds that the radius of curvature is larger than the thickness of the strip in V that is responsible for generating the circulation. In analogy to the second inequality in Lemma 2 we have $|\nabla V|^{-1} < O(\kappa^{-1})$. Then (20) becomes

$$\partial_t(\nabla V)^2 \lesssim c \int_0^t (\nabla V)^3(t')dt', \tag{21a}$$

$$|\nabla V| \lesssim 1/(t^*-t)^2. \tag{21b}$$

This is an alternative reason for our choice of "naive" scaling dimensions in (14).

For the bubble tip in Fig. 4(a) or 11(a), our assumptions of locality, that all the nearby vorticity comes from the parabolic region around the tip and $\kappa/|\nabla V| \lesssim O(1)$, are well satisfied. Vorticity in regions not thereby well represented are far enough away to be treated in a far-field approximation and contribute at most constant stretching since their circulation is bounded by Lemma 2. Therefore

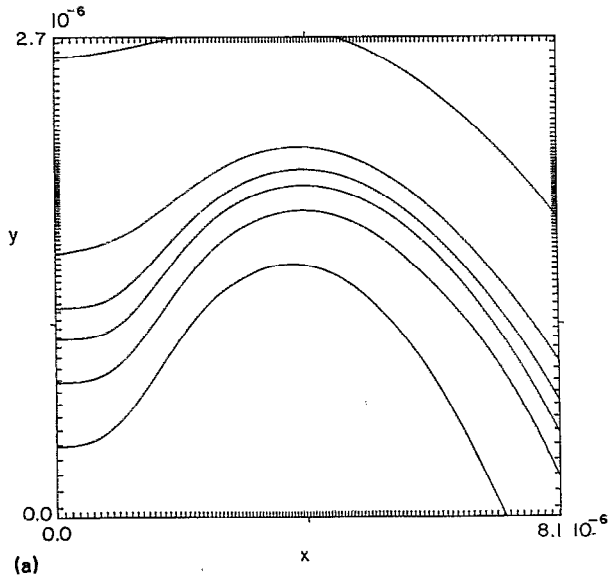

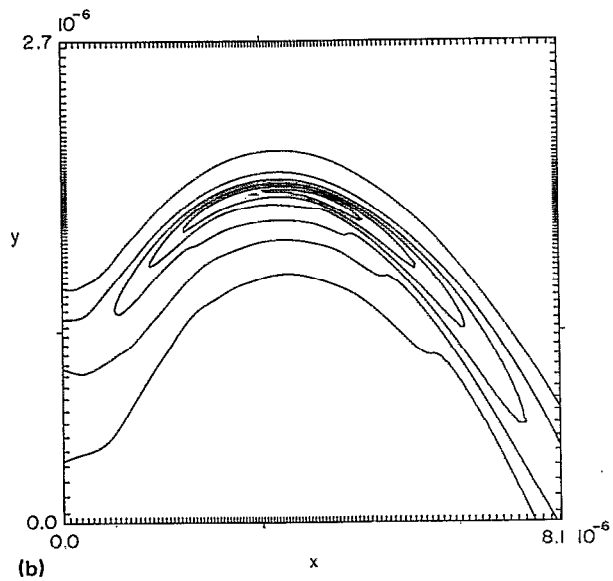

FIG. 20. Continuation of Fig. 19 at $t=10.0780$ (max $|\nabla\theta|=1.1\times10^6$) showing θ in (a), and $|\nabla\theta|$ in (b) with y magnified relative to x. The contour lines in (a) run from 0.88 to 0.48 in units of 0.08 and those in (b) from 1.795×10^5 to 1.077×10^6 in units of 1.795×10^5. The origin in x has been shifted from Fig. 19.

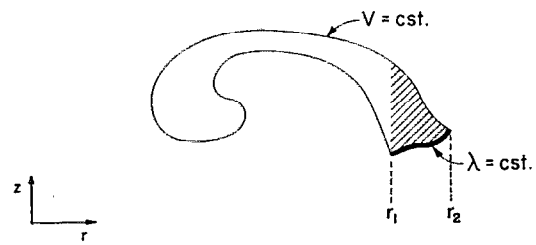

FIG. 21. Illustration of an arbitrary Lagrangian contour used in Lemma 2 to show that the circulation of Ω is only produced from the shaded triangle according to Eq. (7b).

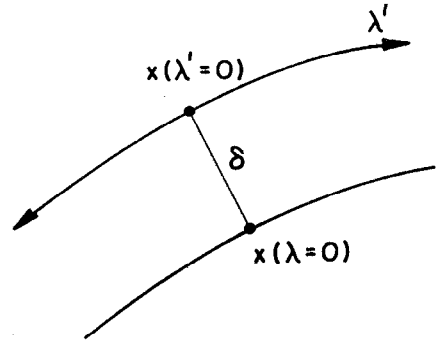

FIG. 22. Illustration of the coordinates employed to calculate the strain produced by the step in V^2 labeled by λ' at a point on another step [cf. Eq. (19)].

the tip must become unstable (cf. Sec. V B below) before any blowup can occur since otherwise (20) predicts exponential growth.

Equation (20) is clearly a poor approximation to the strain in the center of a spiral such as Fig. 4(a) or 6(a), because there is vorticity nearby in space that is comparatively distant when measured along a contour line. Let us define the spiral as a ribbon bounded by a given contour line of V. We can then assert by Lemma 2 that the total circulation is bounded. (With some control on the shearing of the $\lambda=cst$ lines one could assert that the circulation density, $\partial_\lambda C$, decreases with the stretching, but that we will not need.)

To bound the strain in (18) it suffices to put x in the center of the spiral and approximate the spiral as a series of concentric uniform, rings of width w_i and radius $r_i=\Sigma_{j=1}^{i}w_j$. Take the absolute value of the integrand in (18), replace the integral of $d\lambda'$ around one ring by $(d\lambda'/ds)(2\pi r_i)$ where s is arclength, and in the center let $1/(x-x')^2\to1/r_i^2$. The inverse stretching $d\lambda'/ds$ is related by volume conservation to $|\nabla V|^{-1}$ which in turn varies as w_i. After amalgamating all constants into c, our bound on (18) becomes

$$\hat{n}\cdot e\cdot\hat{n}<c\sum_{i=1}^{N}\frac{w_i}{r_i}<c'\ln\left(\frac{r_N}{\min_i(w_i)}\right) \tag{22}$$

with the restriction that the r_N is fixed. Although r_N may grow, it will do so only at some smooth rate determined by the large scales and therefore it remains finite at any hypothetical blowup time. The second inequality follows by extremizing over all w_i. For $G=\max_i|\nabla V|^2\sim1/\min_i(w_i)^2$ we find from (16)

$$\partial_t G<cG\ln G$$

and no finite time singularity.

B. Linear stability of the bubble cap

In our axisymmetric simulations, instabilities never appeared in the thin spherical caps [cf. Fig. 11(a)] and we need to verify for our parameters that none are expected.

We also show that the instability which is already well developed in Fig. 14(a) indeed occurred where expected. Since the axisymmetric problem was run for many times the characteristic Rayleigh–Taylor time scale for a flat interface, with no superimposed flow, the strain-induced stability of Zeldovich *et al.*,[9] discussed by many authors,[10] is probably responsible for stabilizing the bubble.

In view of the figures, it is reasonable to idealize the bubble as a wedge cut from a circle and introduce the thickness of the interface between hot and cold only as a lower cutoff on the minimum allowed wavelength. Following WKB, we will linearize (15) around the straight interface

$$r=r_0,$$

$$z(\lambda)=l\lambda,$$

where l is a characteristic length; for a bubble, the radius of curvature is r_c. A constant strain, $s>0$, defined as

$$v_r=-s(r-r_0),$$

$$v_z=sz,$$

is superimposed on the interface and we initialize with $r=r_0+a\cos(k\lambda)$, $a\ll 1$ and $\gamma=0$. The circulation builds up as $\gamma=-k\sin(k\lambda)\int_0^t a(t')dt'$ and for $a(t)$ we find

$$\ddot{a}+2s\dot{a}+(s^2-\sigma^2e^{-st})a=0, \tag{23}$$

where $\sigma^2=\frac{1}{2}gk/l$. We have checked numerically that (23) can be solved accurately enough for our purposes with a WKB ansatz, $a(t)=\exp[\int_0^t f\,(t')dt']$ with

$$f=-s+\sigma e^{-st/2}.$$

Clearly the shortest wavelengths grow most rapidly but provided the perturbation remains small, it will eventually decay because the stretching increases its wavelength and decreases its amplitude. The maximum of $a(t)$ works out to be just $a(0)(s^2/\sigma^2)\exp[2(\sigma/s-1)]$. To decide in a practical sense whether a given bubble ($l\to r_c$) is stable, take the maximum $k=r_c/\delta$, where δ is the thickness, and demand amplification by a factor r_c/δ, i.e., a perturbation of magnitude some fraction of δ grows to the same fraction of r_c. Our criterion for instability is

$$\left(\frac{r_c}{\delta}\right)\left(\frac{g}{2\delta s^2}\right)\lesssim\exp 2\left[\left(\frac{g}{2\delta s^2}\right)^{1/2}-1\right]. \tag{24a}$$

We evaluated (24a) at $t=17$ in Fig. 9 which is the last point of the solid curve. At this time, $g=\Delta V^2/r_0^3\sim 8^2/13^3$, $r_c\sim 1$, $r_c/\delta\sim 15$, and around the tip $s=0.5$, so that $g/(2\delta s^2)\sim 0.9$ and (24a) is not satisfied. For the Boussinesq simulation around $t\sim 7.5$ we have $g=1$ by assumption, $r_c\sim 2.0$, $r_c/\delta\simeq 50$, and $s=0.5$ again, so that (24a) is easily satisfied.

A more refined approximation models the bubble as a curved slab of thickness Δ, $\delta\ll\Delta\ll r_c$, obtained by intersecting a wedge with an annulus. To be conservative, we terminate the unstable growth when ke^{-st} decreases from r_c/δ to Δ/δ, but otherwise repeat the derivation of (24a). One finds for instability,

$$\left(\frac{\Delta r_c}{\delta^2}\right)\lesssim\exp 2\left\{\left(\frac{g}{2\delta s^2}\right)^{1/2}\left[1-\left(\frac{\delta}{\Delta}\right)^{1/2}\right]\right\}, \tag{24b}$$

which is still satisfied in the Boussinesq simulation since $\delta/\Delta\sim 0.25$.

Note that as $\delta\to 0$ even with Δ/δ fixed, an arbitrary amount of amplification [e.g. the right-hand side of (24b)] occurs before the wavelength is stretched out to r_c. This alone would not demonstrate linear instability, in a strict sense, for perturbations around a precisely stationary state (i.e., a flat interface extending to infinity), but the bubble is by no means a stationary flow and there are multiple sources for the initial perturbation assumed in deriving (24a) and (24b).

VI. CONCLUSION

Let us recapitulate the evidence in favor of a finite time singularity for the axisymmetric Euler equations. After the contour lines of θ near $x=0$ went from convex to concave and cusp like ($t\gtrsim 8.5$ in Fig. 12), an additional 10^4 increase in $\max(|\nabla\theta|)$ was observed with no obvious impediment to further integration. A far better diagnostic for a finite time singularity is the strain evaluated where $|\nabla\theta|$ is maximum, i.e., $\partial_t \ln\max(|\nabla\theta|)$. Exponential growth in $\max(|\nabla\theta|)$ is thereby reduced to a constant. There is every indication in Fig. 13(b) that the inverse strain will hit zero in a finite time.

The most questionable aspect of our numerics is the nearly uniform increment of strain that gets lost when circulation is pushed out to infinity. This could be readily parametrized and compensated for by adding a uniform strain by hand each time modes were truncated at infinity. This would eliminate the steps from Fig. 13(b) and very plausibly hasten the collapse. While this may be done in the future, the methodology we have followed provides explicit and public bounds on our sins.

It should be emphasized that this collapse problem cannot be touched without an adaptive mesh code. Our final inner mesh spacing was $\sim 2\times 10^{-8}$, and the initial data had an outer scale $\gtrsim 1$. To even proceed as far as the initial instability in Fig. 14 requires a grid spacing of $\lesssim 10^{-3}$.

The data in Fig. 13, plus the slow decrease in θ across the interface noted at the end of Sec. IV C, are all consistent with the scaling forms (v is velocity),

$$\theta=cst+\tau^{\eta}f\,[\mathbf{x}/\tau^{2+\eta},-\ln(\tau)], \tag{25a}$$

$$\mathbf{v}=cst+\tau^{1+\eta}\mathbf{h}[\mathbf{x}/\tau^{2+\eta},-\ln(\tau)], \tag{25b}$$

where $\tau=t^*-t$ and the dependence of f,h on the rescaled time $T\sim-\ln(\tau)$ must be slower than exponential for the prefactors to be well defined. In fact f and $\mathbf{h}$ remain $O(1)$ as $T\to\infty$. A fit gives $\eta=0.2\pm 0.1$ if only random errors are included and perhaps ± 0.2 if systematic errors are factored in. It is very unlikely, particularly in view of the similar results we obtain for porous media convection [cf. Eq. (27) below] that there is not some decrease in θ as $T\to\infty$. Obviously for our range of scales, a small exponent cannot be distinguished from a logarithm.

The attentive reader will have noted in connection with [Eq. (10a)] that a more general symmetry of the Boussinesq equation is

$$\theta \to cst + l^{\eta}\theta(\mathbf{x}/l^{2+\eta}, t/l),$$

$$\omega \to \frac{1}{l}\,\omega\left(\frac{\mathbf{x}}{l^{2+\eta}}, \frac{t}{l}\right), \tag{26}$$

where l and η are constants. The relative scalings on θ, x, and t are dictated by the dimensions of the effective gravitational acceleration. It is (26) of course which underlies (25). Hence the continuous rescaling in (10a)–(10c) merely removed the largest part of the divergence. Additional small coordinate adjustments were still made by hand as already noted. A more elaborate algorithm in which both η and α [cf. (10c)], were adjusted could be implemented but was not worth the effort.

The inattentive reader will by now have observed in (25b) that the singular part of the velocity decreases, but clearly the vorticity and strain still diverge as τ^{-1}. The same is true of the inviscid Burgers' equation at the point of shock formation.

The $-\ln(\tau)$ argument in (25) is essential since the shape of the solution is continuously evolving and shows no signs of stabilizing. It is entirely plausible to us that this is real and just a manifestation of repeated Rayleigh–Taylor instabilities and roll-up. Looked at more closely, the growth appears in bursts with each new instability causing enhanced stretching, which is stabilizing, until the interface thins sufficiently for a new instability to occur. It should be emphasized that singularities may occur essentially independently all along the bubble interface since the dynamics are local. The same phenomena was seen in our earlier simulations of vortex filaments.[11]

It clearly makes sense to ask if f and $\mathbf{h}$ in (25) have chaotic dynamics as a function of $T \sim -\ln(\tau)$. Our numerics are inconclusive on this point since four decades of scaling in length translate to very few characteristic times in T. To prove that a singularity exists would require showing that η and α could be adjusted in equations for f and $\nabla \wedge \mathbf{h}$ analogous to (10b) so as to obtain smooth $O(1)$ solutions. In contrast to a fixed point, a chaotic flow in T, even if low dimensional, greatly complicates this task. There may be some narrow window on the orbit through which the scaled solution can leak away. On the other hand, chaotic flows have embedded unstable periodic points which could be searched for numerically.

It is useful to contrast our conclusions with two other singularity problems in two dimensions. A vortex sheet is known to have a finite time curvature singularity with the time-integrated stretching, $\partial_\lambda s$, uniformly bounded.[12] This depends crucially on the zero thickness limit being taken first and is not relevant to a situation like ours with smooth initial data in which for a sheet approximation to be valid, $\kappa^{-1} \gtrsim \text{thickness} \sim (\partial_\lambda s)^{-1}$. (Area preservation relates the thickness and stretching.)

Another relevant problem is porous media convection[13] that is defined by a conserved scalar $\mu(\mathbf{x},t)$ evolving under

$$\partial_t \mu + \mathbf{v}\cdot\nabla\mu = 0, \quad v = \mu\hat{x}_1 - \nabla\phi, \quad \nabla^2\phi = \partial_1\mu, \tag{27}$$

where the velocity $\mathbf{v}$, and not its time derivative, is determined by the buoyancy force $\mu\hat{x}_1$. The corresponding interface model is still (15) with no time history, i.e., $\gamma = \partial_\lambda x_1$.

Extensive simulations have shown that μ "falls" or "rises," depending on its sign, in the x_1 direction and makes a sharp interface which proceeds to randomly fold in such a way that $\kappa/\partial_\lambda s$ is bounded between two constants. There is a finite time singularity obeying $\partial_\lambda s \sim |\nabla\mu| \sim 1/(t^* - t)$ and a very slow decay in the jump of μ across the interface. The fluctuations in the scaling regime are more pronounced than seen here.

Let us finally translate back from Boussinesq to three-dimensional axisymmetric variables and note several conclusions. The enstrophy from a single singularity is bounded, but $\int |\boldsymbol{\omega}|^{2+a}\, d^3\mathbf{x}$ with $a > \eta$ diverges. This follows from $\omega_{r,z} \sim \tau^{-2}$ and the length scale $\tau^{2+\eta}$ [in (25)] applied to δr and δz [cf. the transition from (6) to (7)]. [The energy in the singular region scales as $\tau^{4+4\eta}$ and comes from v_ϕ, i.e., (25a).] This is of course a weaker blowup than expected dimensionally for the unconstrained Euler equations, $\boldsymbol{\omega} \sim \tau^{-1} g(x/\tau)$, because the singular region is smaller. Note also that a larger prefactor, τ^{-2} vs τ^{-1}, for instance, is a sign that the governing equation is less nonlinear (i.e., consider solutions to $d_t x = x^{1+a}$). The small singular region also makes the singularity easily controlled by viscosity. Simple dimensional considerations give a viscous length which scales as $\nu^{(2+\eta)/(3+2\eta)}$ in terms of the kinematic viscosity ν.

We are inclined to believe that nonsymmetric singularities exist in three dimensions and are either unstable or appear on smaller scales than were reached in Ref. 2. To elucidate the precise mechanisms would be very interesting. The singularities we have uncovered here are without much physical relevance and would be unstable if the axisymmetry were relaxed.

Of more immediate interest is to realize how the "conventional" vorticity strain relation emerges for axisymmetric flow.[14,15] Recall that the rate of strain matrix in the high dissipation regions has eigenvalues of signs $(+,+,-)$. The intermediate one is much less than the others and the vorticity is parallel to it. The same picture emerged for the bubble cap which acts as a vortex sheet with $\boldsymbol{\omega}$ along $\hat{z}$, across which v_ϕ has a large jump (i.e., the flow is locally a two-dimensional shear). The existence of the bubble follows simply from the Boussinesq analogy, but an argument of comparable physical appeal is unknown in three dimensions.

In the vicinity of the vortex maximum, most of the initial conditions studied in Ref. 2 are locally axisymmetric in the sense that the tip of a parabola can be approximated by a circle. This could partially account for the genesis of the vortex sheets observed there. In conformity with our observations in Ref. 2, nonzero net helicity did not have a qualitative impact on the flow structures (cf. Sec. IV A).

Note added in proof. Slightly more extensive Bouss-

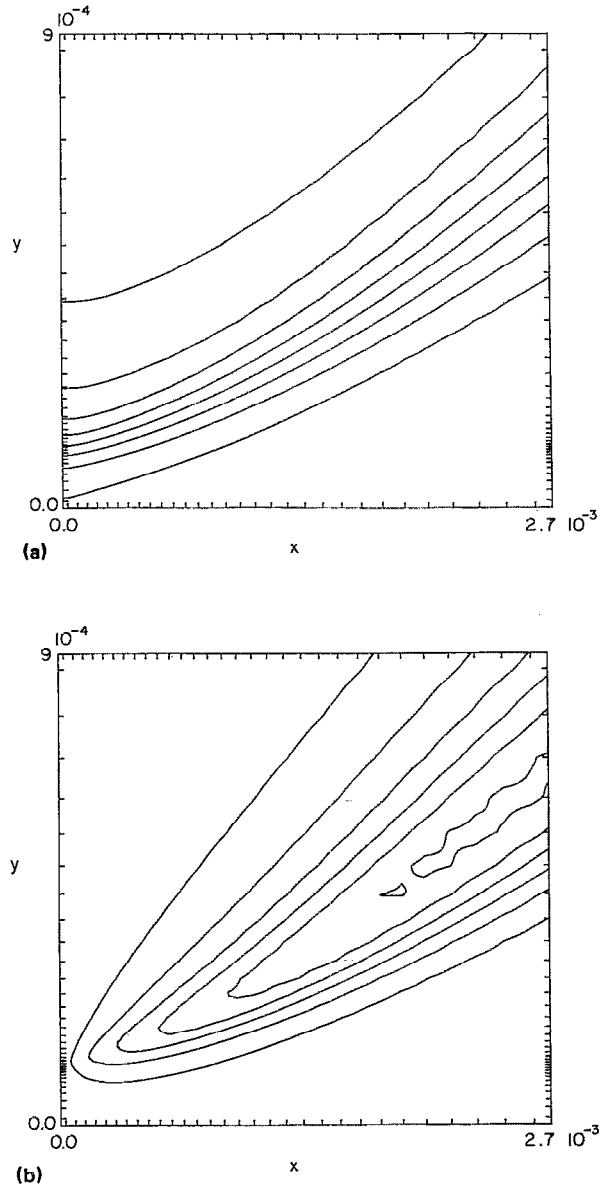

FIG. 23. The temperature θ (a) and vorticity ω (b) for a 128^2 mesh corresponding to the final time in Table I.

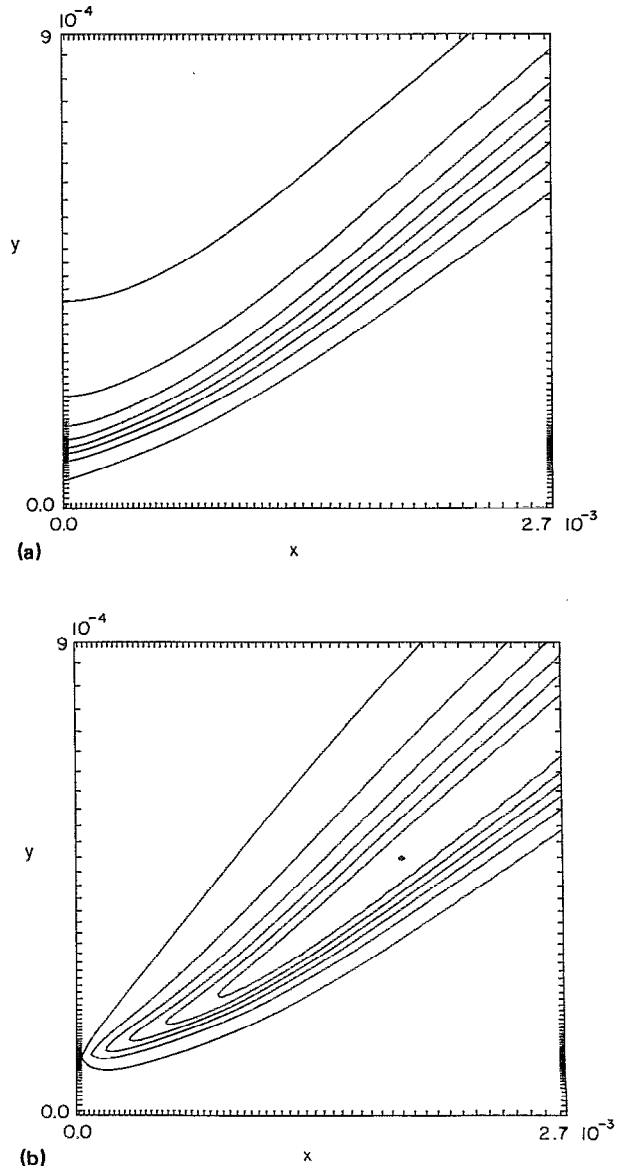

FIG. 24. The same data as in Fig. 23 except on a 256^2 mesh.

inesq simulations than those presented here have appeared in Ref. 16.

ACKNOWLEDGMENTS

We are indebted to Grauer and Sideris, who first searched for the singularities in axisymmetric flow, for communicating their results to us, although we found their numerical evidence unpersuasive.[17] G. Baker, R. Caflisch, and T. Dombre also made useful comments. C. B. Laney provided essential guidance on the subtleties of finite-difference schemes for problems involving sharp fronts. Our computations were done on RISC 6000 workstations donated by IBM.

Support was provided by the Air Force Office of Scientific Research under Grant No. 91-0011 and the National Science Foundation under Grant No. DMR-9012974.

APPENDIX: MESH REFINEMENT

In this section we compare our numerical scheme on four different meshes, 128^2, 192^2, 256^2, and 384^2 for the Boussinesq equations (10a)–(10c). (Note that Figs. 12–20 were obtained for 256^2.) For each factor of 2 in resolution, our computer time increases by 10, a factor of 4 to 5 for the Poisson inversion, and a factor 2 for the time step which is set by the Courant condition. We restarted our data near the middle of the scaling regime where $|\nabla\theta| \sim 3000$ [cf. Figs. 12 and 13(a)], and ran it through two remeshes during which time $\max|\nabla\theta|$ grew by a factor of ~ 3.9. Filtering was done on the first remesh, when the number of mesh points was changed, but not on the second to accentuate

TABLE I. Convergence of maximum vorticity (first entry) and maximum $|\nabla\theta|$ with mesh. The entry marked "growth" is the ratio of line 3 to line 1. The last line is the strain rate at the final time at the point where $|\nabla\theta|$ is maximum. All runs were begun by remeshing a common file at $t=9.845$ doing a second remesh at the same resolution at $t=9.916$, and continuing to $t=9.959$. The integration was done with Eqs. (10a)–(10c).

Time	128^2	192^2	256^2	384^2
Remesh 1	(85.1, 2350)	(89.6, 2650)	(92.1, 2850)	(93.8, 3110)
Remesh 2	(89.5, 4430)	(104, 5620)	(111, 6160)	(119, 6850)
Final	(103, 6650)	(127, 9640)	(144, 1.10×10^4)	(163, 1.26×10^4)
Growth	(1.21, 2.83)	(1.42, 3.64)	(1.56, 3.86)	(1.74, 4.05)
Strain	15.0	15.8	16.6	15.9

any numerical noise. The initial data resembled Fig. 16 with the "Vee" a bit more developed.

Before considering the data, one limitation should be stressed. We are simulating a system that plausibly has a positive Lyapunov exponent. Small errors will grow exponentially as in any other chaotic or turbulent system. One typically assumes that the system tends to an attractor, and that statistical averages are reproducible numerically. We have redone, in various segments, all the data in Fig. 12 for $|\nabla\theta|_{\max} \gtrsim 10^2$ experimenting with coordinates and various ways of remeshing. The contour plots are always very close for comparable values of $|\nabla\theta|_{\max}$ and the largest percentage error is in the time a certain instability induced pattern forms. The scaling behavior in Figs. 13(a) and 13(b) is robust.

Figures 23 and 24 show the data for the 128^2 and 256^2 meshes at the final time in Table I. In comparison with Fig. 24, the initial data was similar in shape and less well resolved by a factor of $\sim 2/3$, which places it at the low end of our acceptable range. Resolution is always defined by the number of grid points per say a factor two change in θ near the origin. At the final time, there are no obvious numerical instabilities visible in the 128^2 data which has simply been diffused more in the high gradient region by the TVD algorithm.

In Table I, the first row shows purely the errors attributable to describing a continuous field with a discrete mesh plus the filtering that was done after interpolation. The percentage errors in max ω are smaller than $|\nabla\theta|$ since the latter involves a derivative and converges only as mesh spacing squared. To estimate the errors for 256^2 we compared with data initialized onto a 512^2 mesh (which we could not afford to run further), which gave $\max(\omega, |\nabla\theta|) = (94.7, 3230)$ and therefore errors of $\sim(3\%, 12\%)$. [Without the initial filtering, the errors are $(<1\%, 7\%)$.]

After time evolution, the errors in $|\nabla\theta|$ reflect what was seen in the figures. Clearly the errors grow in time as one expects. Normalized to a factor 2 increase in $|\nabla\theta|$ and extrapolated to reflect our actual mesh, 256^2, versus infinity we obtain errors $\sim(10\%, 5\%)$, which is comparable to what was quoted in Sec. IV. Most of the error in the third line of Table I is attributable to the initial conditions. The errors in ω relative to $|\nabla\theta|$ are larger than expected since its maxima occurs in a less well-resolved region of the flow. Also, examination of the 384^2 contour plots suggests that the incipient roll-ups visible in Figs. 18(c) and 18(d) occur sooner for higher resolution as is physically reasonable.

The strain as noted earlier is $\sim 2d\ln(|\nabla\theta|)/dt$. Hence the last line in Table I shows that in spite of the greater diffuseness of the vorticity on the coarser mesh, the growth rate of the singularity is not greatly affected. The large disparities in $|\nabla\theta|$ at the final time are not due to the comparatively small errors in the intrinsic growth rate but rather the enhanced diffusivity generated by the TVD algorithm on a coarser mesh and the initial conditions. Evidently, the true solution diverges more rapidly than the numerical one.

[1] R. Grauer and T. Sideris (private communication); "Numerical computation of three dimensional incompressible ideal fluids with swirl," Phys. Rev. Lett. **67**, 3511 (1991). They find the largest vorticity at a point well removed from the plume tip and employ less resolution that we found necessary to reach our first instability (cf. Fig. 14).

[2] A. Pumir and E. D. Siggia, "Collapsing solutions to the 3-D Euler equations," Phys. Fluids A **2**, 220 (1990).

[3] S. Kline, W. Reynolds, F. Schraub, and P. Runstadler, "The structure of turbulent boundary layers," J. Fluid Mech. **30**, 741 (1967).

[4] M. Brachet, D. Meiron, B. Nickel, S. Orszag, and U. Frisch, "Small scale structure of the Taylor–Green vortex," J. Fluid Mech. **130**, 411 (1983); M. Brachet (private communication).

[5] For a general discussion see C. B. Laney and D. A. Caughey, "Extremum control II: Semidiscrete approximations to conservation law," AIAA Paper No. 91-0632, 1991.

[6] S. Osher and S. Chakravarty, "High resolution schemes and the entropy condition," SIAM J. Numer. Anal. **21**, 955 (1984).

[7] P. N. Swartzrauber, "A direct method for the discrete solution of separable elliptic equations," SIAM Rev. **19**, 490 (1977).

[8] D. McLaughlin, G. Papanicolaou, C. Sulem, and P. Sulem, "Focusing singularity of the cubic Schrödinger equation," Phys. Rev. A **34**, 1200 (1986).

[9] Ya. B. Zeldovich, A. G. Istratov, N. I. Kidin, and V. B. Librovich, "Flame propagation in tubes: Hydrodynamics and stability," Combust. Sci. Technol. **24**, 1 (1985).

[10] P. Pelcé and P. Clavin, "The stability of curves fronts," Europhys. Lett. **3**, 907 (1987); G. K. Batchelor, "The stability of a large gas bubble moving through a liquid," J. Fluid Mech. **184**, 399 (1987).

[11] A. Pumir and E. D. Siggia, "Vortex dynamics and the existence of solutions to the Navier–Stokes equations," Phys. Fluids **30**, 1606 (1987).

[12] D. W. Moore, "The spontaneous appearance of a singularity in the shape of an evolving vortex sheet," Proc. R. Soc. London Ser. A **365**, 105 (1979); D. Meiron, G. Baker, and S. Orszag, "Analytic structure of vortex sheet dynamics 1. Kelvin–Helmholtz instability," J. Fluid Mech. **114**, 283 (1982).

[13] A. Pumir, B. I. Shraiman, and E. D. Siggia, "Vortex morphology and Kelvin's theorem," Phys. Rev. A **45**, R5351 (1992).

[14] E. D. Siggia, "Numerical study of small-scale intermittency in three dimensional turbulence," J. Fluid Mech. **107**, 357 (1982), where the vorticity–strain correlation functions were calculated.

[15] W. Ashurst, A. Kerstein, R. Kerr, and C. Gibson, "Alignment of vorticity and scalar gradient with strain in simulated Navier–Stokes turbulence," Phys. Fluids **30**, 2343 (1987).

[16] A. Pumir and E. D. Siggia, "Finite time singularities in the axisymmetric three dimensional Euler equations," Phys. Rev. Lett. **68**, 1511 (1992).

[17] Axisymmetric simulations, generally comparable to our own, prior to turning to the Boussinesq approximation, have been reported by D. Meiron and M. Shelley (private communication).